

1 **Rheologic constraints on the upper mantle from five years of**
2 **postseismic deformation following the El Mayor-Cucapah**
3 **earthquake**

4 **T. T. Hines¹, E. A. Hetland¹**

5 ¹Department of Earth and Environmental Sciences, University of Michigan, Ann Arbor, Michigan, USA.

6 **Key Points:**

- 7 • Transient postseismic deformation can be observed following the El Mayor-Cucapah
8 earthquake at epicentral distances of up to 400 km
9 • Near-field postseismic deformation exhibits early transience that decays to a sustained
10 rate which is elevated above the preseismic trend
11 • Far-field postseismic deformation can be explained with a Zener or Burgers rheology
12 upper mantle

13 **Abstract**

14 We analyze five years of Southern California GPS data following the Mw=7.2 El Mayor-
 15 Cucapah earthquake. We observed transient postseismic deformation which persists for three
 16 years at epicentral distances greater than ~ 200 km. In the near-field, rapid postseismic trans-
 17 sience decays to a sustained rate which exceeds its pre-earthquake trend. We attempt to de-
 18 termine the mechanisms driving this deformation, where we consider afterslip at seismogenic
 19 depths and viscoelastic relaxation in the lower crust and upper mantle as candidate mechanisms.
 20 We find that early, rapid, near-field deformation can be explained with afterslip on the fault
 21 that ruptured coseismically, while the later, sustained, near-field deformation can be explained
 22 with either continued afterslip in an effectively elastic lower crust, or lower crustal viscoelas-
 23 tic relaxation with a steady-state viscosity of $\sim 10^{19}$ Pa s. The trend in far-field deformation
 24 is best explained with a transient viscosity of $\sim 10^{18}$ Pa s in the upper mantle. We argue that
 25 a transient rheology in the mantle is preferable over a Maxwell rheology because it better pre-
 26 dicts the decay in postseismic deformation, and also because it does not conflict with the gen-
 27 erally higher, steady-state viscosities inferred from studies of geophysical processes occurring
 28 over longer time-scales.

29 **1 Introduction**

30 Ground deformation in the years following a large ($Mw \gtrsim 7$) earthquake can be used to
 31 gain insight into the mechanical behavior of the crust and upper mantle. The interpretations
 32 of postseismic deformation are not always conclusive because multiple postseismic deforma-
 33 tion mechanisms, such as afterslip or viscoelastic relaxation in the lower crust and upper man-
 34 tle, can have qualitatively similar surface expressions [e.g. Savage, 1990]. This complication
 35 can potentially be remedied by having a sufficient number of well positioned observations of
 36 the postseismic displacement field [Hearn, 2003]. Owing to the dense geodetic network de-
 37 ployed throughout the 2000s as part of the Plate Boundary Observatory, the postseismic de-
 38 formation following the April 4, 2010, Mw=7.2 El Mayor-Cucapah earthquake in Baja Cal-
 39 ifornia was observed at more GPS stations than any other earthquake in California to date (see
 40 Hauksson *et al.* [2011] and Fletcher *et al.* [2014] for a detailed description of this earthquake
 41 and its seismotectonic context). With such a large collection of data, we attempt to discern the
 42 mechanisms driving postseismic deformation following the El Mayor-Cucapah earthquake.

43 Previous studies which have modeled postseismic deformation following the El Mayor-
 44 Cucapah earthquake include Pollitz *et al.* [2012], Gonzalez-Ortega *et al.* [2014], Spinler *et al.*
 45 [2015], and Rollins *et al.* [2015]. Of these studies, Gonzalez-Ortega *et al.* [2014] and Rollins
 46 *et al.* [2015] have attempted to describe the postseismic deformation with afterslip in an elas-
 47 tic half-space. Gonzalez-Ortega *et al.* [2014] described five months of postseismic deforma-
 48 tion, observed by InSAR and GPS stations within ~ 50 km of the rupture, with afterslip and
 49 contraction on the coseismically ruptured fault. Gonzalez-Ortega *et al.* [2014] noted that their
 50 preferred model underestimated the GPS displacements for stations $\gtrsim 25$ km from the rup-
 51 ture and suggested that it could be the result of unmodeled viscoelastic relaxation. Using only
 52 continuous GPS stations, which are mostly north of the rupture zone, Rollins *et al.* [2015] found
 53 that three years of postseismic deformation can be adequately explained by afterslip, albeit with
 54 an implausibly large amount of slip inferred on the least constrained, southern-most fault seg-
 55 ment. Here, we suggest the afterslip inferred by Rollins *et al.* [2015] may have been acting as
 56 a proxy for distributed relaxation in the upper mantle.

57 Pollitz *et al.* [2012], Rollins *et al.* [2015] and Spinler *et al.* [2015] have explored viscoelas-
 58 tic relaxation in the lower crust and upper mantle as a potential postseismic deformation mech-
 59 anism. The rheology of the crust and mantle is largely unknown and so modeling postseis-
 60 mic deformation with viscoelastic relaxation requires one to assume a rheologic model and
 61 then find the best fitting rheologic parameters. The inference of these rheologic parameters is
 62 a computationally expensive non-linear inverse problem which is typically approached with
 63 a forward modeling grid search method. Consequently, a simplified structure for the Earth must

be assumed in order to minimize the number of rheologic parameters that need to be estimated. For example, it is commonly assumed that the lower crust and upper mantle are homogeneous, Maxwell viscoelastic layers, which may be too simplistic for postseismic studies [Riva and Govers, 2009; Hines and Hetland, 2013]. To further reduce the dimensions of the model space, it is also necessary to make simplifying assumptions about the behavior of afterslip. For example, one can assume a frictional model for afterslip and parametrize afterslip in terms of the unknown rheologic properties of the fault [e.g. Johnson *et al.*, 2009; Johnson and Segall, 2004]. One can also assume that afterslip does not persist for more than a few months and then model the later postseismic deformation assuming it to be the result of only viscoelastic relaxation [e.g. Pollitz *et al.*, 2012; Spinler *et al.*, 2015]. However, postseismic afterslip in similar tectonic settings has been observed to persist for decades following earthquakes [Cakir *et al.*, 2012; Cetin *et al.*, 2014]. Indeed, the preferred viscoelastic model from Pollitz *et al.* [2012] significantly underestimates deformation in the Imperial Valley, which could be indicative of unmodeled continued afterslip. Neglecting to allow for sustained afterslip as a postseismic mechanism could then lead to biased inferences of viscosities.

In this study, we perform a kinematic inversion for fault slip, allowing it to persist throughout the postseismic period, while simultaneously estimating the viscosity of the lower crust and upper mantle. We create an initial model of the fault slip and effective viscosity necessary to describe early postseismic deformation using the method described in Hines and Hetland [2016]. This method uses a first-order approximation of surface deformation resulting from viscoelastic relaxation which is only applicable to the early postseismic period. In this case, our initial model describes the first 0.8 years of postseismic deformation following the El Mayor-Cucapah earthquake. We then use the inferred effective viscosity structure from the initial model to create a suite of postseismic models to explain the five years of postseismic data available to date. Of the suite of models tested, we find that postseismic deformation following the El Mayor-Cucapah earthquake can be explained with a combination of afterslip on a fault segment running through the Sierra Cucapah and viscoelastic relaxation in a Zener rheology upper mantle with a transient viscosity on the order of 10^{18} Pa s.

2 Data Processing

We use continuous GPS position time series provided by University Navstar Consortium (UNAVCO) for stations within a 400 km radius about the El Mayor-Cucapah epicenter. We collectively describe the coseismic and postseismic displacements resulting from the El Mayor-Cucapah earthquake as $u_{\text{post}}(t)$. We consider the GPS position time series, $u_{\text{obs}}(t)$, to be the combination of $u_{\text{post}}(t)$, secular tectonic deformation, annual and semi-annual oscillations, and coseismic offsets from significant earthquakes over the time span of this study. The June 14, 2010, Mw=5.8 Ocotillo earthquake and the Brawley swarm, which included an Mw=5.5 and an Mw=5.4 event on August 26, 2012, (Figure 1) are the only earthquakes that produced noticeable displacements in any of the time series. We treat the displacements resulting from the Brawley swarm as a single event because the daily solutions provided by UNAVCO cannot resolve the separate events. Although the Ocotillo earthquake had its own series of aftershocks [Hauksson *et al.*, 2011], neither the Ocotillo earthquake nor the Brawley swarm produced detectable postseismic deformation. We model displacements resulting from these events with only a Heaviside function, $H(t)$, describing the coseismic offsets. We then model $u_{\text{obs}}(t)$ as

$$u_{\text{obs}}(t) = u_{\text{pred}}(t) + \epsilon, \quad (1)$$

where

$$\begin{aligned} u_{\text{pred}}(t) = & u_{\text{post}}(t)H(t - t_{\text{emc}}) + c_0 + c_1 t + \\ & c_2 \sin(2\pi t) + c_3 \cos(2\pi t) + c_4 \sin(4\pi t) + c_5 \cos(4\pi t) + \\ & c_6 H(t - t_{\text{oc}}) + c_7 H(t - t_{\text{bs}}). \end{aligned} \quad (2)$$

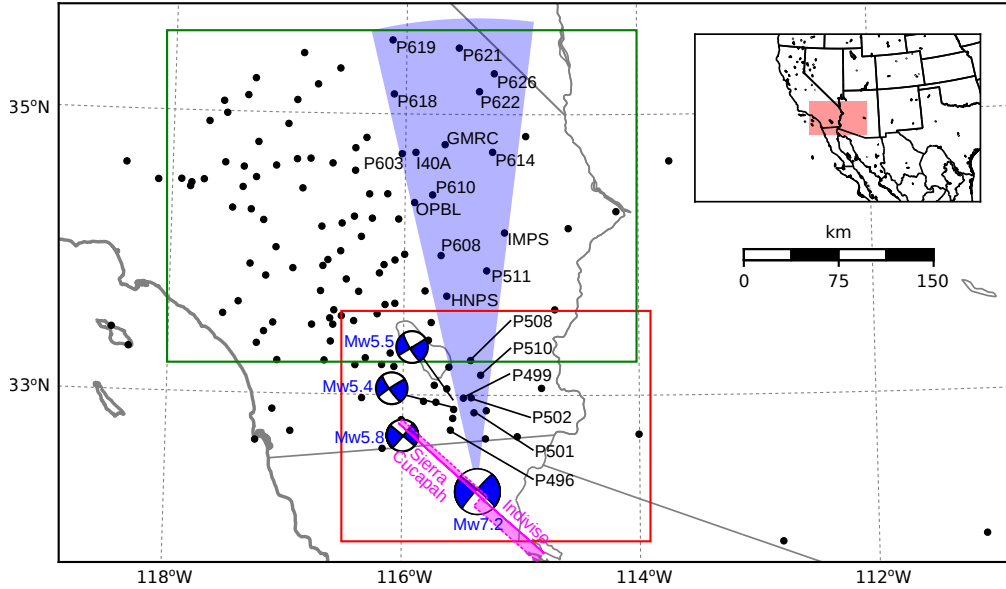


Figure 1. Map of the region considered in this study. The large focal mechanism is the GCMT solution for the El Mayor-Cucapah earthquake, and the three small focal mechanisms are for the Ocotillo earthquake and the two main shocks during the Brawley swarm. The black dots indicate the locations of GPS stations used in this study. The fault geometry used in this study is shown in magenta where dashed lines indicate buried edges of the fault segments. The green and red boxes demarcate the extent of the near-field and far-field maps (Figures 4 and 5). Stations inside the blue sector, which highlights the area within 10° of the El Mayor-Cucapah P-axis, are used in Figures 7 and 10.

In the above equations, t_{emc} , t_{oc} and t_{bs} are the times of the El Mayor-Cucapah earthquake, Ocotillo earthquake, and the Brawley swarm, respectively, c_0 through c_7 are unknown coefficients, and ϵ is the observation noise. We are using years as our unit of time which makes c_2 through c_5 the coefficients for annual and semi-annual oscillations. We only estimate jumps associated with the Ocotillo earthquake and Brawley swarm for stations within 40 km of their epicenters.

Stations which recorded displacements that clearly cannot be described by the aforementioned processes are not included in our analysis. This includes stations in the Los Angeles basin, where anthropogenic deformation can be larger than the postseismic signal that we are trying to estimate [Bawden *et al.*, 2001; Argus *et al.*, 2005]. In order to ensure an accurate estimation of the secular deformation, we only use stations that were installed at least six months prior to El Mayor-Cucapah earthquake even though several GPS stations were installed after the earthquake to get better coverage of the postseismic deformation field [Spiner *et al.*, 2015]. It would be possible to subtract secular velocities derived from elastic block models [e.g. Meade and Hager, 2005] from velocities recorded at the newly installed stations to get an estimate of postseismic velocities at those stations. However, estimating velocities from an already noisy displacement time series can introduce significant uncertainties depending on exactly how the estimation is done. We therefore use coseismic and postseismic displacements, rather than velocities, in our inverse method described in Section 3. This choice prevents us from using the newly installed stations for our analysis.

The October 16, 1999, Mw=7.1 Hector Mine earthquake, which occurred \sim 270 km north of the El Mayor-Cucapah epicenter, produced transient postseismic deformation which we do not wish to model, either mechanically or through empirical line fitting. We thus restrict our analysis to deformation observed six years after the Hector Mine earthquake, which is when

139 postseismic velocities at sites near the Hector Mine epicenter are approximately constant [Savage
 140 and Svare, 2009]. When appraising our model fit in Section 3, we see some systematic
 141 residuals in the vicinity of the Hector Mine epicenter, which may be the result of errors in the
 142 assumption that the trend in Hector Mine postseismic deformation is linear after six years.

143 Studies of postseismic deformation typically assume a parametric form for $u_{\text{post}}(t)$, such
 144 as one with a logarithmic or exponential time dependence [e.g. Savage *et al.*, 2005]. However,
 145 by assuming a logarithmic or exponential form of $u_{\text{post}}(t)$ we run the risk of over fitting the
 146 GPS time series and inferring a non-existent postseismic signal. We therefore do not assume
 147 any parametric form for $u_{\text{post}}(t)$ and rather treat it as integrated Brownian motion, so that

$$\dot{u}_{\text{post}}(t) = \sigma^2 \int_0^t w(s)ds, \quad (3)$$

148 where $w(t)$ is white noise and the variance of $\dot{u}_{\text{post}}(t)$ increases linearly with time by a factor
 149 of σ^2 . We use a Kalman filtering approach to estimate $u_{\text{post}}(t)$ and the unknown parameters
 150 in eq. (2). In the context of Kalman filtering, our time varying state vector is

$$\mathbf{X}(t) = [u_{\text{post}}(t), \dot{u}_{\text{post}}(t), c_0, \dots, c_7] \quad (4)$$

151 and eq. (2) is the observation function which maps the state vector to the GPS observations.
 152 We initiate the Kalman filter by assuming a prior estimate of $\mathbf{X}(t)$ at the first time epoch, denoted
 153 $\mathbf{X}_{1|0}$, which has a sufficiently large covariance, denoted $\Sigma_{1|0}$, to effectively make our
 154 prior uninformed. For each time epoch, t_i , Bayesian linear regression is used to incorporate
 155 GPS derived estimates of displacement with our prior estimate of the state, $\mathbf{X}_{i|i-1}$, to form
 156 a posterior estimate of the state, $\mathbf{X}_{i|i}$, which has covariance $\Sigma_{i|i}$. We then use the posterior
 157 estimate of the state at time t_i to form a prior estimate of the state at time t_{i+1} through the
 158 transition function

$$\mathbf{X}_{i+1|i} = \mathbf{F}_{i+1} \mathbf{X}_{i|i} + \delta_{i+1}, \quad (5)$$

159 where

$$\mathbf{F}_{i+1} = \begin{bmatrix} 1 & (t_{i+1} - t_i) & \mathbf{0} \\ 0 & 1 & \mathbf{0} \\ \mathbf{0} & \mathbf{0} & \mathbf{I} \end{bmatrix} \quad (6)$$

160 and δ_{i+1} is the process noise, which has zero mean and covariance described by

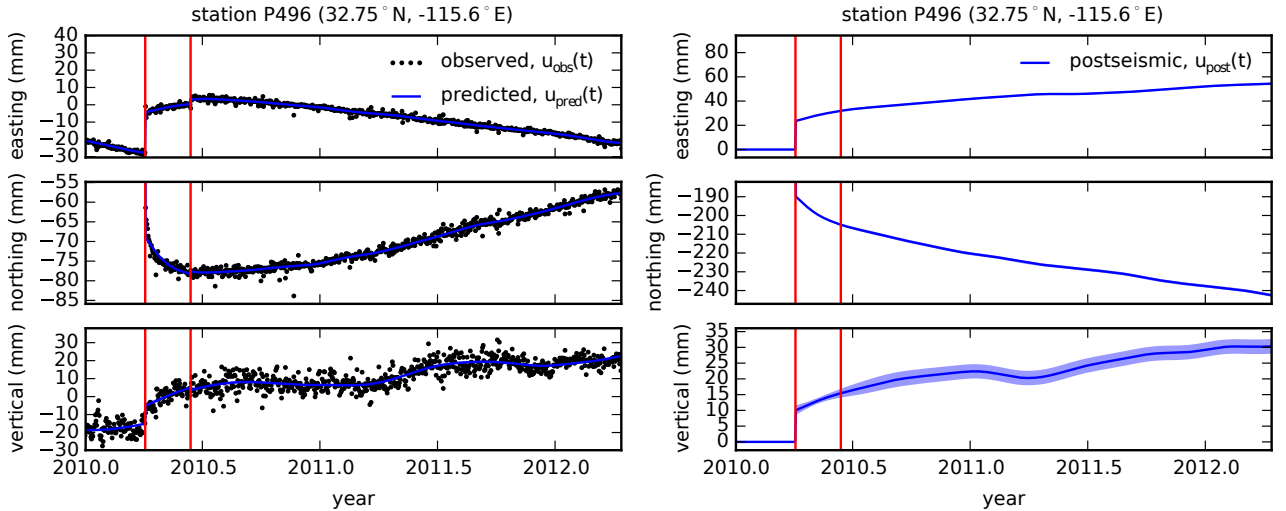
$$\mathbf{Q}_{i+1} = \sigma^2 \begin{bmatrix} \frac{(t_{i+1}-t_i)^3}{3} & \frac{(t_{i+1}-t_i)^2}{2} & \mathbf{0} \\ \frac{(t_{i+1}-t_i)^2}{2} & (t_{i+1} - t_i) & \mathbf{0} \\ \mathbf{0} & \mathbf{0} & \mathbf{0} \end{bmatrix}. \quad (7)$$

161 The covariance of the new prior state, $\mathbf{X}_{i+1|i}$, is then described by

$$\Sigma_{i+1|i} = \mathbf{F}_{i+1} \Sigma_{i|i} \mathbf{F}_{i+1}^T + \mathbf{Q}_{i+1}. \quad (8)$$

162 This process is repeated for each of the N time epochs at which point we use Rauch-Tung-
 163 Striebel smoothing [Rauch *et al.*, 1965] to find $\mathbf{X}_{i|N}$, which is an estimate of the state at time
 164 t_i that incorporates GPS observation for all N time epochs. Our final estimates of $u_{\text{post}}(t)$
 165 are used in subsequent analysis, while the remaining components of the state vector are con-
 166 sidered nuisance parameters. In the interests of computational tractability, we down sample
 167 our smoothed time series from daily solutions down to weekly solutions.

168 The smoothness of $u_{\text{post}}(t)$ is controlled by the chosen value of σ^2 , which describes how
 169 rapidly we expect postseismic displacements to vary over time. Setting σ^2 equal to zero will



186 **Figure 2.** Left panels show GPS time series from UNAVCO (black) and the predicted displacement (blue)
 187 from eq. (2) for a near-field station. Red lines indicate the times of the El Mayor-Cucapah and Ocotillo earth-
 188 quake. The right panels show estimated coseismic and postseismic displacements u_{post} which are extracted
 189 from the predicted displacements. The 68% confidence interval is shown in light blue.

170 effectively result in modeling $u_{\text{post}}(t)$ as a straight line which is insufficient to describe the
 171 expected transient behavior in postseismic deformation. The other end member, where σ^2 is
 172 infinitely large, will result in $u_{\text{pred}}(t)$ over fitting the data. While one can use a maximum like-
 173 lihood based approach for picking σ^2 [e.g. Segall and Mathews, 1997], we instead take a sub-
 174 jective approach and choose a value for σ^2 that is just large enough to faithfully describe the
 175 observed deformation at the most near-field station in our study, P496, which exhibits the most
 176 rapid changes in velocity. This ensures that σ^2 will be sufficiently large so that our estimate
 177 of $u_{\text{post}}(t)$ does not smooth out potentially valuable postseismic signal at the remaining sta-
 178 tions. We find that using $\sigma^2 = 0.05 \text{ m}^2/\text{yr}^3$ adequately describes all but the first week of post-
 179 seismic deformation at station P496, which slightly increases our estimate of coseismic dis-
 180 placements (Figure 2). We include an example of estimating $u_{\text{post}}(t)$ for a far-field station,
 181 P619, which is about 359 km north of the El Mayor-Cucapah epicenter (Figure 3). At station
 182 P619, along with all the other stations in the Mojave region, there is a south-trending post-
 183 seismic transience that persists for the first three years after the El Mayor-Cucapah earthquake.
 184 Postseismic deformation that extends to these epicentral distances has also been observed af-
 185 ter the Hector Mine earthquake [Freed et al., 2007].

191 It is important to note that the shown uncertainties in $u_{\text{post}}(t)$ do not account for the non-
 192 negligible epistemic uncertainty in eq. (2). For example, we assume a constant rate of secu-
 193 lar deformation, which appears to be an appropriate approximation for all but perhaps the sta-
 194 tions closest to the Hector Mine epicenter, as noted above. Also, our model for seasonal de-
 195 formation in eq. (2) assumes a constant amplitude over time, which means that any yearly vari-
 196 ability in the climatic conditions could introduce systematic residuals [Davis et al., 2012]. In-
 197 deed, it would be more appropriate to consider the seasonal amplitudes $c_2 - c_5$ in eq. (2) as
 198 stochastic variables [Murray and Segall, 2005]. By using constant seasonal amplitudes, our es-
 199 timate of $u_{\text{post}}(t)$ seems to describe some of the unmodeled annual and semi-annual oscilla-
 200 tions (e.g. Figure 3).

201 We show in Figures 4 and 5 the near and far-field postseismic displacements accumu-
 202 lated over the time intervals 0–1 years, 1–3 years, and 3–5 years, as well as the coseismic dis-
 203 placements. Stations at epicentral distances beyond ~ 200 km have an elevated rate of defor-
 204 mation for the first three years following the earthquake. This far-field deformation is trend-

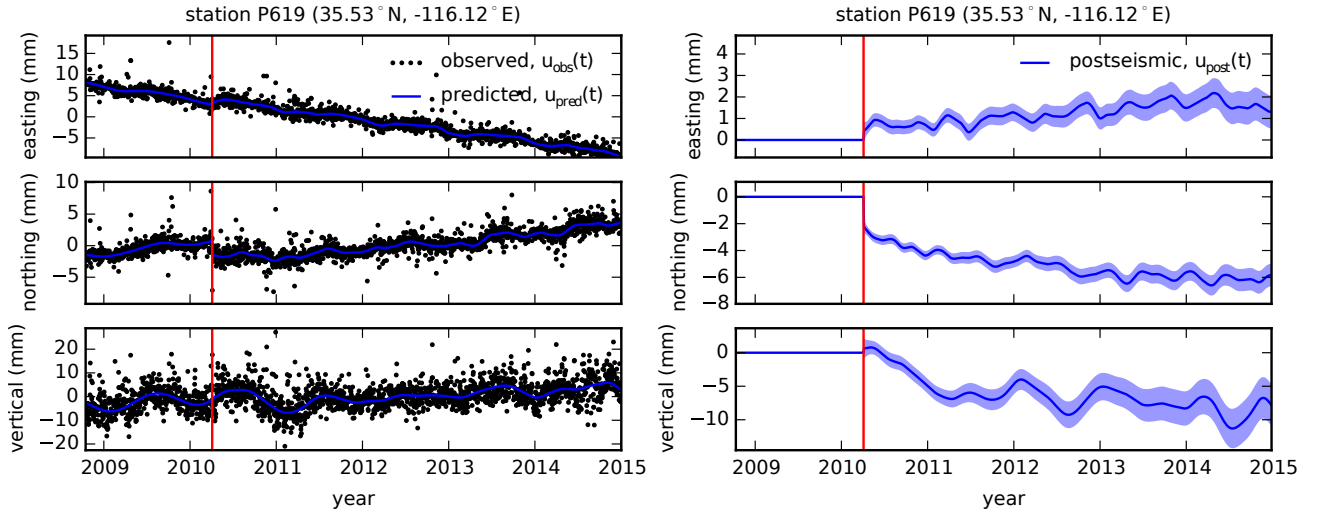


Figure 3. same as Figure 2 but for a far-field station.

ing southward at a rate of a few millimeters per year along the direction of the El Mayor-Cucapah P-axis. A similar eastward trend can be seen in the few far-field stations in Arizona, located along the T-axis. After three years, the trend in far-field postseismic deformation is barely perceptible. Most far-field stations display an initial subsidence for the first year after the El Mayor-Cucapah earthquake followed by continued uplift. This trend in vertical deformation can be observed in all three of the quadrants where postseismic data is available, which means that the vertical deformation does not exhibit an anti-symmetric quadrant pattern, as would be expected for postseismic processes. Although we use vertical deformation in our analysis in Section 3, we do not put an emphasis on trying to describe the vertical deformation because it likely does not have postseismic origins.

The near-field postseismic deformation is notably sustained when compared to the far-field deformation. Namely, the station in this study which is closest to the El Mayor-Cucapah epicenter, P496, has a steady postseismic trend of ~ 1.5 cm/yr to the south after about one year. Vertical postseismic deformation in the near-field does display a quadrant pattern which is consistent with the coseismic vertical deformation, suggesting that it is resulting from postseismic processes. However, the vertical postseismic signal is only apparent for the first year after the earthquake (Figure 4). As with the far-field deformation, there is a general trend of uplift in the near-field after about one year.

3 Postseismic Modeling

We seek to find the mechanisms driving five years of postseismic deformation following the El Mayor-Cucapah earthquake and we consider afterslip and viscoelastic relaxation as candidate mechanisms. Poroelastic rebound has also been used to model postseismic deformation [e.g. Jónsson *et al.*, 2003]; however, Gonzalez-Ortega *et al.* [2014] found that poroelastic rebound is unlikely to be a significant contributor to postseismic deformation following the El Mayor-Cucapah earthquake. Furthermore, we consider stations which are sufficiently far away from the rupture that poroelastic rebound should be insignificant.

We estimate coseismic and time-dependent postseismic fault slip, both of which are assumed to occur on a fault geometry modified from Wei *et al.* [2011b]. Field studies [Fletcher *et al.*, 2014] and LIDAR observations [Oskin *et al.*, 2012] have revealed a significantly more complicated fault geometry than what was inferred by Wei *et al.* [2011b], especially within the Sierra Cucapah. However, we find that a relatively simple coseismic fault geometry based on

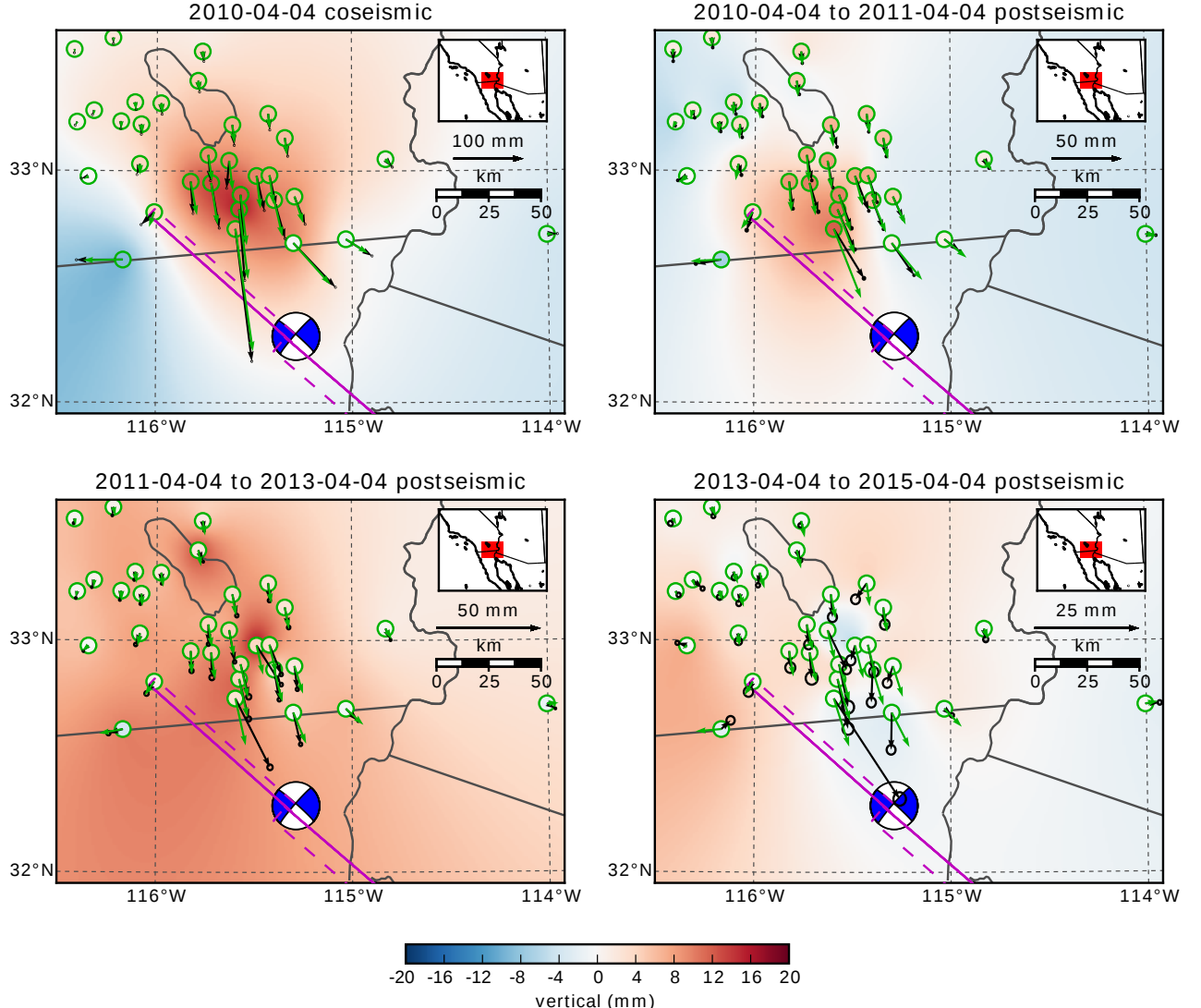
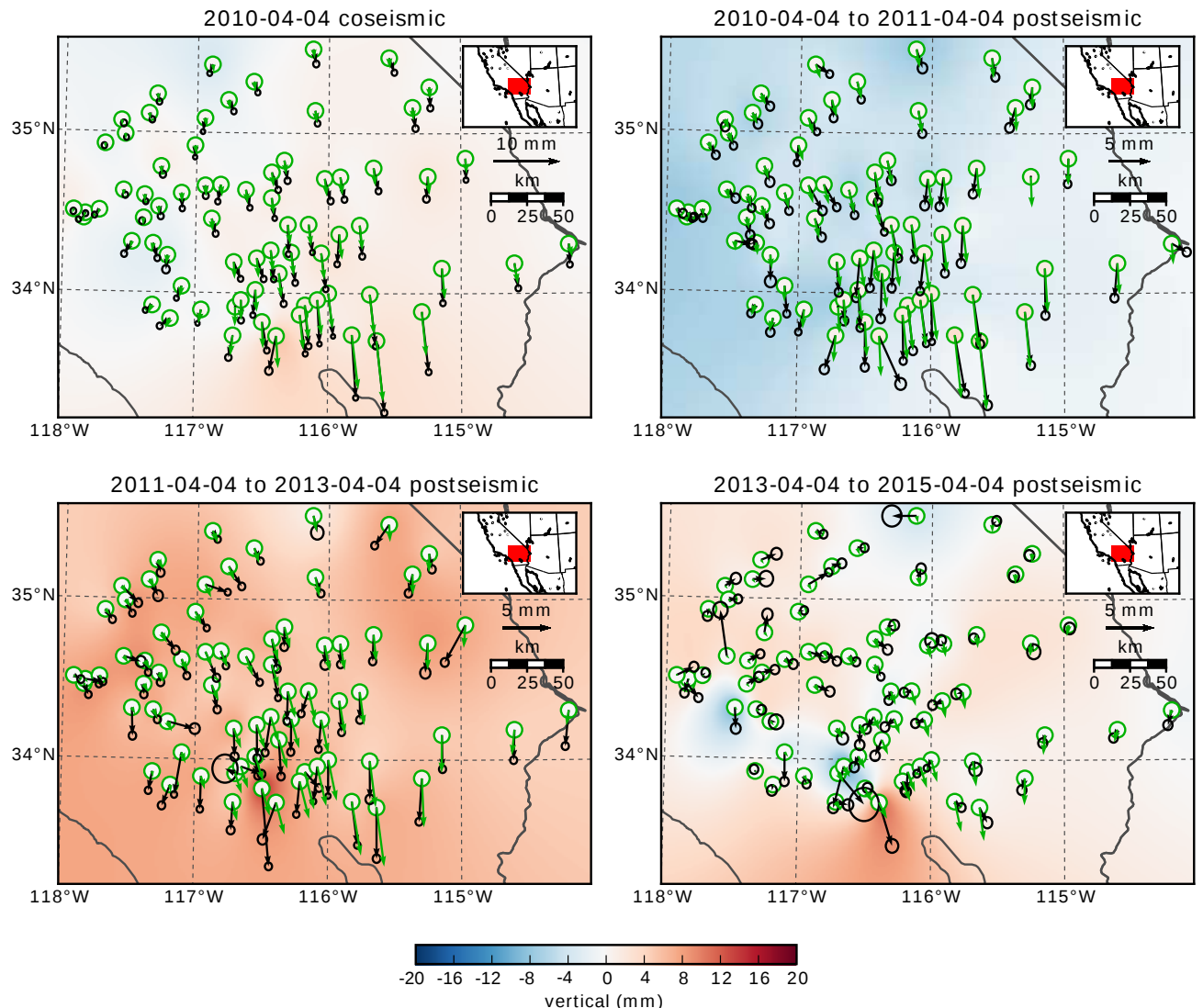


Figure 4. Near-field coseismic and cumulative postseismic displacements over the indicated time periods (black) and predicted displacements for our preferred model from Section 3.3 (green). Observed vertical displacements are shown as an interpolated field and predicted vertical displacements are shown within the green circles. Note that the interpolant is not well constrained in Mexico where there is no data available.

depth (km)	λ (GPa)	μ (GPa)	η_{eff} (10^{18} Pa s)	μ_k/μ
0-5	24.0	24.0	-	-
5-15	35.0	35.0	-	-
15-30	42.0	42.0	44.3	0.0
30-60	61.0	61.0	5.91	0.375
60-90	61.0	61.0	1.99	0.375
90-120	61.0	61.0	1.31	0.375
120-150	61.0	61.0	1.10	0.375
150- ∞	61.0	61.0	1.07	0.375

Table 1. Assumed and estimated material properties. λ and μ are assumed known *a priori* and are based on the values used for the coseismic model by Wei *et al.* [2011b]. The values for η_{eff} are estimated in Section 3.2, and μ_k/μ are the optimal shear moduli ratios found in Section 3.3 for a Zener rheology upper mantle.

**Figure 5.** Same as Figure 4 but for far-field stations.

219

[Wei *et al.*, 2011b] is adequate because most of the stations used in this study are sufficiently far from the El Mayor-Cucapah rupture zone that they are insensitive to the details in the fault geometry found by Fletcher *et al.* [2014] and Oskin *et al.* [2012]. The fault geometry used in this study (Figure 1) consists of the two main fault segments inferred by Wei *et al.* [2011b], where the northern segment runs through the Sierra Cucapah up to the US-Mexico border and the southern segment is the Indiviso fault which extends down to the Gulf of California. Both segments extend from the surface to 15 km depth. We extend the northern segment by 40 km to the northwest, motivated by the clustering of aftershocks on the northern tip of the coseismic rupture zone [Hauksson *et al.*, 2011; Kroll *et al.*, 2013]. This extended fault segment was also found to be necessary by Rollins *et al.* [2015] and Pollitz *et al.* [2012] in order to describe the postseismic deformation.

3.1 Elastic Postseismic Inversion

We consider a variety of rheologic models for the lower crust and upper mantle. The simplest rheologic model is to consider them to be effectively elastic and isotropic. In such case, the rheologic parameters consist of the Lamé parameters, λ and μ , which are reasonably well known and we use the same values used by Wei *et al.* [2011b] throughout this paper (Table 1). The only unknown is the distribution of fault slip, which can be easily estimated from postseismic deformation through linear least squares. Using a subset of the GPS stations considered in this study, Rollins *et al.* [2015] found that three years of postseismic deformation following the El Mayor-Cucapah earthquake can be explained with afterslip on the coseismic fault plane without requiring any viscoelastic relaxation. We also perform an elastic slip inversion, but we use GPS stations within a larger radius about the El Mayor-Cucapah epicenter (400 km instead of \sim 200 km). Our forward problem describing predicted postseismic deformation, u_{pred} , in terms of time dependent fault slip, s , is

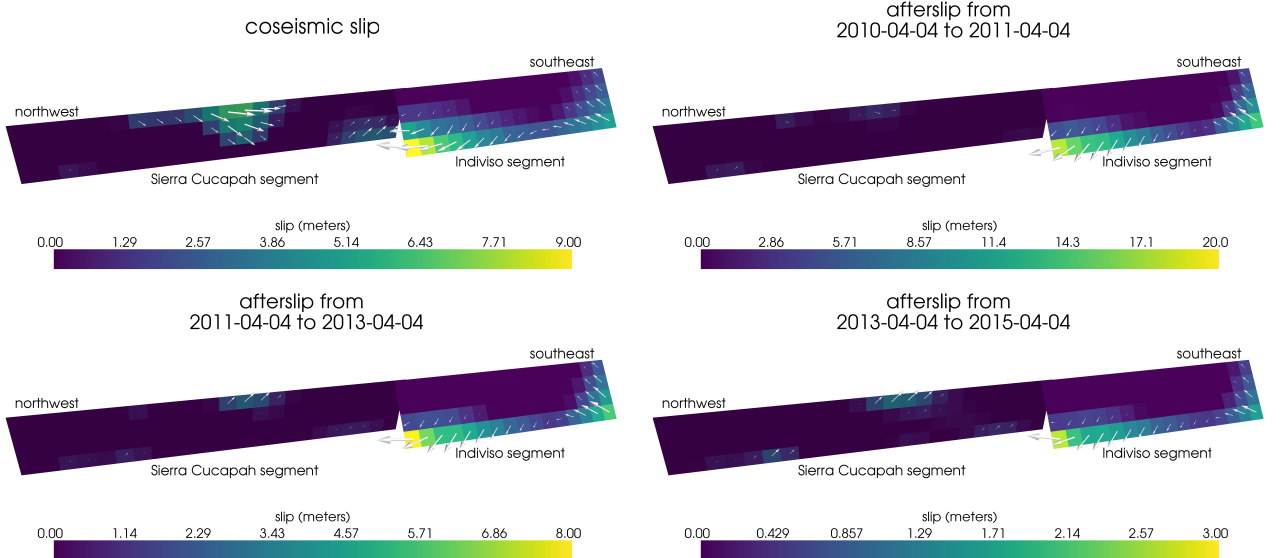
$$u_{\text{pred}}(x, t) = \int_F s(\xi, t) g(x, \xi) d\xi, \quad (9)$$

where F denotes the fault and $g(x, \xi)$ is the elastic Green's function describing displacement at surface position x resulting from slip at ξ on the fault. We estimate coseismic slip and the rate of afterslip over the postseismic time intervals 0.0-0.125, 0.125-0.25, 0.25-0.5, 0.5-1.0, 1.0-2.0, 2.0-3.0, 3.0-4.0, and 4.0-5.0 years. Each fault segment is discretized into roughly 4 km by 4 km patches and we impose that the direction of slip and slip rate are within 45° of right-lateral. We also add zeroth-order Tikhonov regularization so that our solution for s satisfies

$$\min_s \left(\left\| \frac{u_{\text{pred}}(s) - u_{\text{post}}}{\sigma_{\text{post}}} \right\|_2^2 + \lambda_s \|s\|_2^2 \right), \quad (10)$$

where σ_{post} is the uncertainty on postseismic displacements and λ_s is a penalty parameter which is chosen with a trade-off curve. We use Pylith [Aagaard *et al.*, 2013] to compute the Green's functions for this inversion as well as for the remaining inversions in this paper.

Our coseismic slip and afterslip solutions are shown in Figure 6. As with Rollins *et al.* [2015], we find that a large amount of afterslip on the Indiviso fault segment is required to explain the observations. The potency of our inferred coseismic slip is $3.2 \times 10^9 \text{ m}^3$, equivalent to a Mw=7.28 earthquake when assuming a shear modulus of 32 GPa. The potency of our inferred cumulative five years of afterslip is $6.1 \times 10^9 \text{ m}^3$, equivalent to a Mw=7.46 earthquake, which is unrealistically large if we consider afterslip to be driven by coseismically induced stresses. Figure 7 shows the time series for the observed and predicted postseismic displacements at stations along the El Mayor-Cucapah P-axis. We show the radial component of displacements with respect to the El Mayor-Cucapah epicenter and we also rescale the displacements so that the difference between the minimum and maximum observed displacements are the same for each station. Our elastic slip model accurately describes near-field postseis-



294 **Figure 6.** Coseismic slip and cumulative afterslip over the indicated intervals for the elastic model from
295 Section 3.1. Color indicates the magnitude of slip while arrows indicate the motion of the hanging wall.

289 mic deformation and systematically underestimates postseismic deformation at epicentral dis-
290 tances $\gtrsim 150$ km. When the fault segments used in the inversion are extended down to 30 km
291 depth, rather than 15 km, the systematic far-field residuals are smaller but remain apparent.
292 Because an elastic model requires an unrealistic amount of afterslip and is unable to predict
293 far-field deformation, we move on to consider viscoelastic models in the next section.

305 3.2 Early Postseismic Inversion

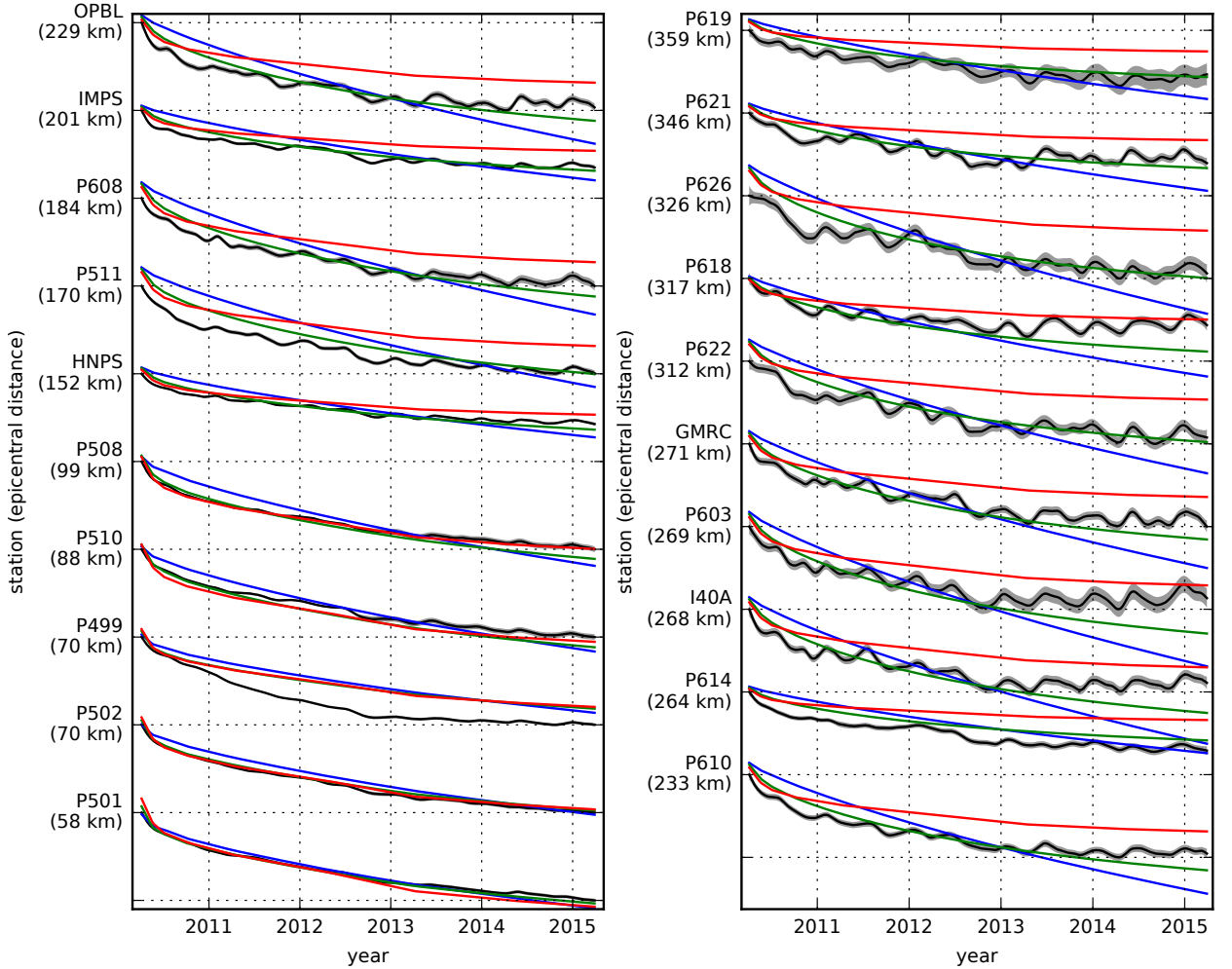
306 For any linear viscoelastic rheology of the crust and mantle, postseismic displacements
307 resulting from time dependent fault slip can be described as

$$u_{\text{pred}}(x, t) = \int_F s(\xi, t) g(x, \xi) d\xi + \int_0^t \int_F s(\xi, \tau) f(t - \tau, x, \xi) d\xi d\tau, \quad (11)$$

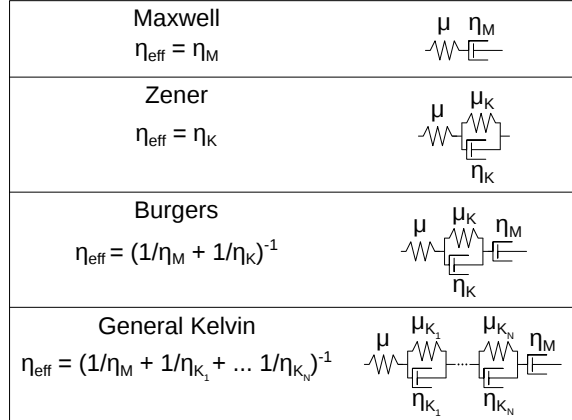
308 where $f(t, x, \xi)$ describes the time-dependent velocity at x resulting from viscoelastic relax-
309 ation of stresses induced by slip at ξ . f is a function of λ , μ , and any additional rheologic pa-
310 rameters controlling the viscoelastic response, which are generally not well known. Schematic
311 representations of the viscoelastic rheologic models considered in this study are shown in Fig-
312 ure 8. We discuss these rheologic models and their use in geophysical studies in Section 4.

315 In order to greatly simplify the inverse problem, we use the method described in *Hines*
316 and *Hetland* [2016] to constrain an initial effective viscosity structure from the early postseis-
317 mic deformation. Our method uses the fact that coseismic stresses throughout the crust and
318 upper mantle depend on the instantaneous elastic parameters and are independent of the vis-
319 coelastic parameters which we wish to estimate. Immediately following an earthquake, each
320 parcel will have a strain rate that is proportional to the coseismic stress and inversely propor-
321 tional to the parcel's effective viscosity, η_{eff} . Using one-dimensional rheologic models, we de-
322 fine the effective viscosity as

$$\eta_{\text{eff}} = \left. \frac{\sigma}{\dot{\varepsilon}} \right|_{t=0}, \quad (12)$$



296 **Figure 7.** Scaled radial component of postseismic displacements. Downward motion indicates that the
 297 station is moving toward the El Mayor-Cucapah epicenter. Displacement time series are scaled so that the
 298 minimum and maximum observed values lie on the grid lines. The observed postseismic displacements, u_{post}
 299 are shown in black with gray indicating the 68% confidence interval. The displacements predicted by the best
 300 fitting elastic model u_{pred} are shown in red. The blue and green lines are the predicted postseismic displace-
 301 ments for the models discussed in Section 3.3. The blue lines show the predicted displacements for the model
 302 with a Maxwell viscoelastic lower crust and upper mantle. The green line shows the predicted displacements
 303 for the model with a Maxwell viscoelastic lower crust and a Zener viscoelastic upper mantle. The effective
 304 viscosities are the same for both models and are shown in Figure 12.



313 **Figure 8.** Schematic illustration of the rheologic models considered in this paper as well as their effective
 314 viscosities.

323 where σ is an applied stress at $t = 0$ and $\dot{\varepsilon}$ is the resulting strain rate. Figure 8 shows how
 324 η_{eff} relates to the parameters for various linear viscoelastic rheologies. We can deduce that the
 325 initial rate of surface deformation resulting from viscoelastic relaxation is a summation of the
 326 surface deformation resulting from relaxation in each parcel, scaled by the reciprocal of the
 327 parcel's effective viscosity. That is to say

$$f(0, x, \xi) = \int_L \frac{h(x, \xi, \zeta)}{\eta_{\text{eff}}(\zeta)} d\zeta, \quad (13)$$

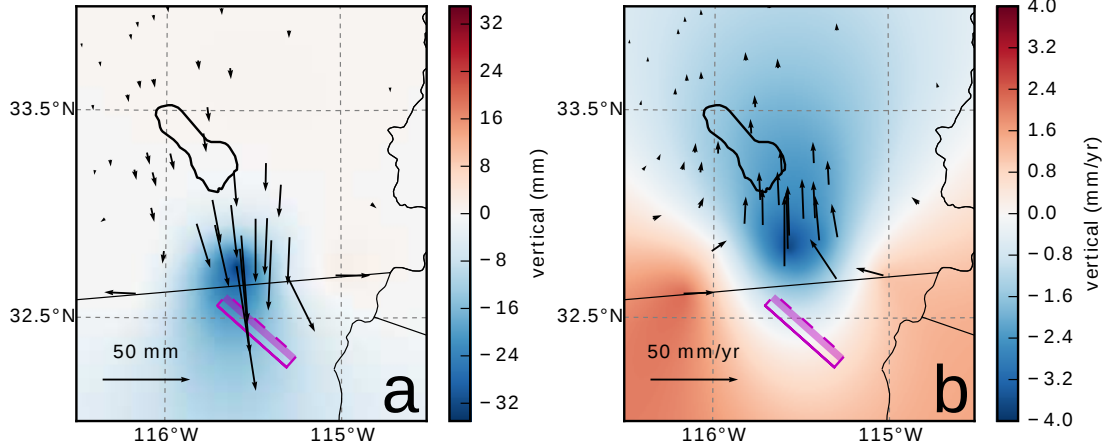
328 where L denotes the crust and mantle and $h(x, \xi, \zeta)$ describes the initial rate of deformation
 329 resulting from viscoelastic relaxation at ζ induced by slip at ξ . We can combine eq. (13) with
 330 eq. (11) to get a first order approximation for early postseismic deformation,

$$u_{\text{pred}}(x, t) \approx \int_F s(\xi, t) g(x, \xi) d\xi + \int_0^t \int_F \int_L \frac{s(\tau, \xi)}{\eta_{\text{eff}}(\zeta)} h(x, \xi, \zeta) d\zeta d\xi d\tau, \quad (14)$$

331 which is valid for as long as the rate of deformation resulting from viscoelastic relaxation is
 332 approximately constant. Although eq. (14) may only be valid for a short portion of the post-
 333 seismic period, its utility becomes apparent when noting that g and h are only functions of
 334 the fault geometry and instantaneous elastic properties, λ and μ , and thus g and h can be com-
 335 puted numerically as a preprocessing step. The forward problem in eq. (14) can then be rapidly
 336 evaluated for any realization of s and η_{eff} . This is in contrast to evaluating the full forward
 337 problem, eq. (11), numerically for each realization of s and the unknown rheologic proper-
 338 ties.

339 Details on how eq. (14) is used to estimate s and η_{eff} from postseismic deformation can
 340 be found in *Hines and Hetland* [2016]. A non-linear Kalman filter based inverse method can
 341 also be used to estimate s and η_{eff} in a manner akin to *Segall and Mathews* [1997] or *McGuire*
 342 and *Segall* [2003], in which we would not have to explicitly impose a time dependent parametriza-
 343 tion of s . We have thoroughly explored Kalman filter based approaches, but we ultimately pre-
 344 fer the method described in *Hines and Hetland* [2016] because of its relative simplicity. More-
 345 over, we believe the piecewise continuous representation of slip with respect to time to be suf-
 346 ficiently general for the resolving power of these GPS data.

347 We estimate coseismic slip and afterslip with the same spatial and temporal discretiza-
 348 tion as in Section 3.1. Simultaneously, we estimate η_{eff} within six vertically stratified layers
 349 which have depths ranging from 15-30 km, 30-60 km, 60-90 km, 90-120 km, 120-150 km,



369 **Figure 9.** Displacements resulting from fault slip at lower crustal depths (a), and initial velocities resulting
 370 from subsequent relaxation of a viscoelastic lower crust (b). The fault segment dips 75° to the north-east and
 371 its surface projection is outlined in magenta. The highlighted area on the fault extends from 15 to 30 km depth
 372 and indicates where 1 meter of right-lateral slip was imposed. The elastic properties of the crust and mantle
 373 are the same as in Table 3, and η_{eff} is 10^{18} Pa s in the lower crust. Vertical displacements are interpolated
 374 between station locations.

350 as well as from 150 km to the bottom of our numerical model domain at 800 km. We again
 351 restrict fault slip to occur between 0 and 15 km depth, which is done in order to help elim-
 352 inate inevitable non-uniqueness in the inversion. It is well understood that fault slip at suffi-
 353 ciently great depths can produce surface deformation that is indistinguishable from viscoelas-
 354 tic relaxation, at least in two-dimensional earthquake models [Savage, 1990]. Additionally, we
 355 note that when simultaneously estimating both afterslip and viscosity in the lower crust, the
 356 inverse problem becomes particularly ill-posed. This ill-posedness is illustrated in Figure 9,
 357 which shows the displacements resulting from a meter of slip on a fault extending from 15
 358 to 30 km depth and the initial velocity resulting from subsequent viscoelastic relaxation in the
 359 lower crust, which is given a viscosity of 10^{18} Pa s. In this demonstration, the viscoelastic re-
 360 laxation is entirely driven by the fault slip in the lower crust. The horizontal displacements
 361 from fault slip are in the opposite direction as the displacements resulting from viscoelastic
 362 relaxation. This means that surface displacements resulting from afterslip at lower crustal depths
 363 can be cancelled out, at least partially, by a low viscosity lower crust. We eliminate this null
 364 space by allowing only one mechanism in the lower crust, which we choose to be viscoelas-
 365 tic relaxation. This is not to say that we do not believe deep afterslip to be a possibility; rather,
 366 we restrict slip to seismogenic depths as a modeling necessity. Although, it has been noted
 367 that the pattern of vertical postseismic deformation following the El Mayor-Cucapah earthquake
 368 indicates that a significant amount of afterslip must be shallow [Rollins et al., 2015].

375 We must determine at which point the early postseismic approximation breaks down, which
 376 we will denote as t_{bd} . As noted, eq. (14) is valid for as long as the rate of deformation re-
 377 sulting from viscoelastic relaxation is approximately constant. We can almost certainly assume
 378 that deformation at the most far-field stations, which are ~ 400 km away from the El Mayor-
 379 Cucapah epicenter, is the result of viscoelastic relaxation. The approximation should then be
 380 valid for as long as a linear trend adequately approximates the far-field deformation. Using
 381 this logic, it would appear that t_{bd} is about one year after the El Mayor-Cucapah earthquake.
 382 Another way to determine t_{bd} is to find the best fitting prediction of eq. (14) to observed de-
 383 formation using increasing durations of the postseismic time series. t_{bd} should be the point
 384 when eq. (14) is no longer capable of describing the observed deformation without incurring
 385 systematic misfits. When using eq. (14) to fit the entire five years of postseismic displacements,

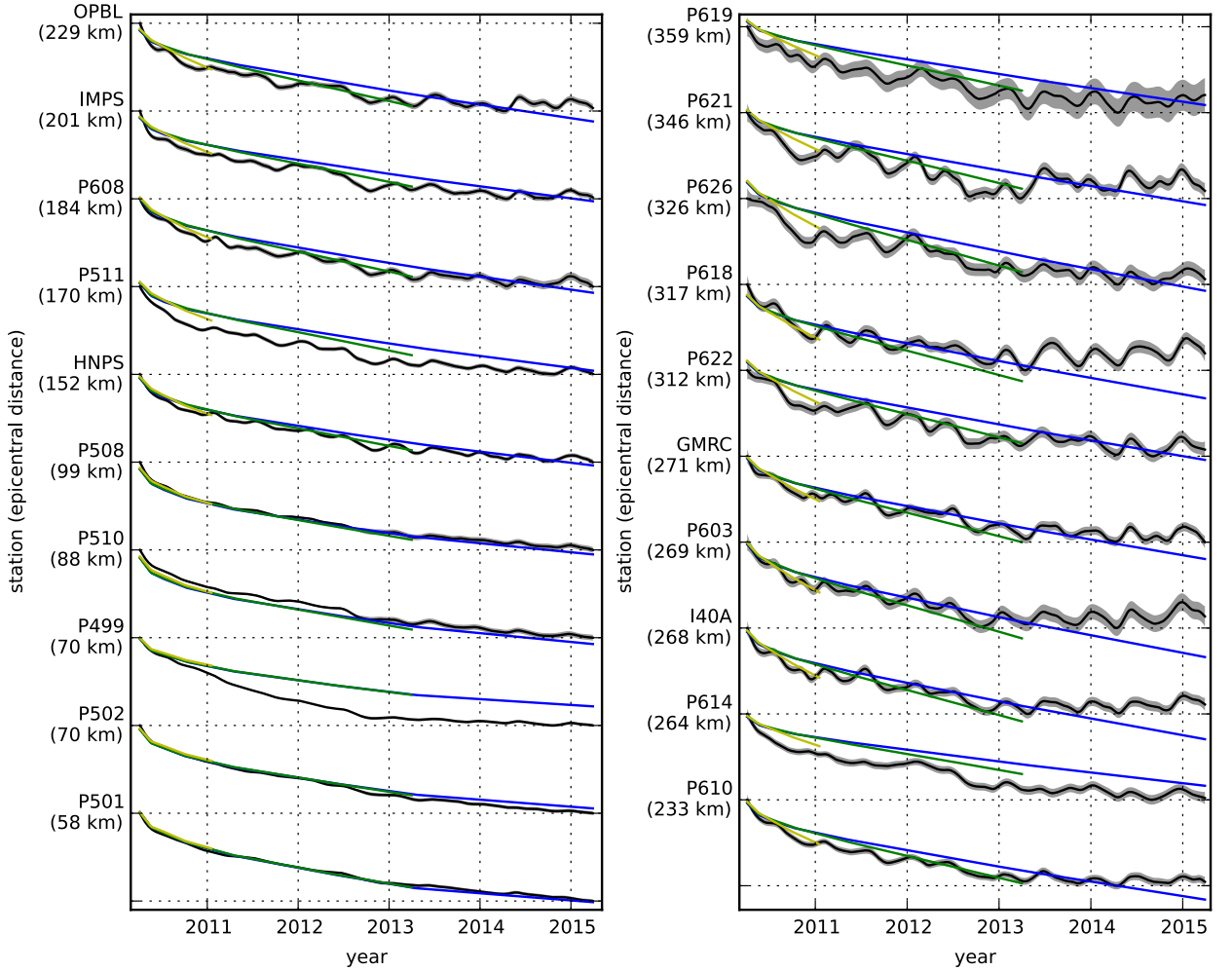


Figure 10. Observed postseismic displacements (black) and best fitting predictions of eq. (14) to 5.0 (blue), 3.0 (green), and 0.8 (yellow) years of the postseismic data.

we see that the near-field displacements (e.g., station P501) are accurately predicted. When looking at displacements in the far-field (e.g., station P621), we see that eq. (14) overestimates the rate of deformation in the later postseismic period and underestimates the rate of deformation in the early period (Figure 10). Due to the low signal-to-noise ratios for far-field stations, it is difficult to determine at what point eq. (14) is no longer able to predict the observed displacements; however, we settle on $t_{bd} = 0.8$ years after the earthquake, while acknowledging that the choice is subjective. As noted in *Hines and Hetland* [2016], overestimating t_{bd} will result in a bias towards overestimating η_{eff} , while picking a t_{bd} which is too low will not necessarily result in a biased estimate of η_{eff} , although the uncertainties would be larger. We can then consider inferences of η_{eff} to be an upper bound on the viscosity needed to describe the far-field rate of deformation during the first 0.8 years of postseismic deformation.

We estimate coseismic slip, afterslip, and effective viscosities by solving

$$\min_{s, \eta_{eff}} \left(\left\| \frac{u_{pred}(s, \eta_{eff}) - u_{post}}{\sigma_{post}} \right\|_2^2 + \lambda_s \|s\|_2^2 + \lambda_\eta \|\nabla \eta_{eff}^{-1}\|_2^2 \right), \quad (15)$$

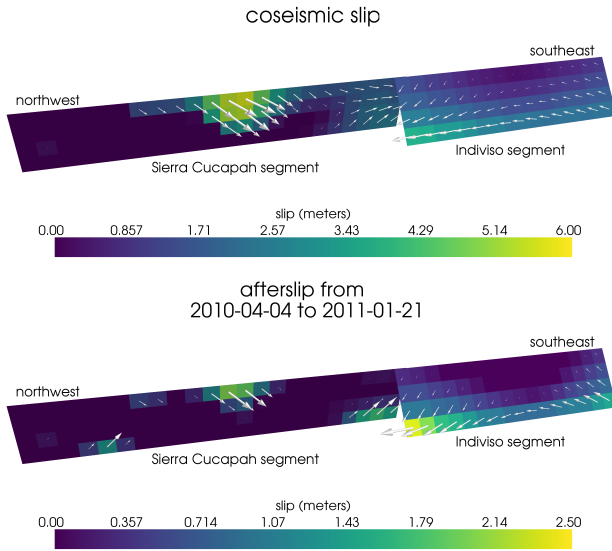
400 where u_{post} consists of the first 0.8 years of postseismic deformation and u_{pred} are the pre-
 401 dicted displacements from eq. (14). Due to inherent non-uniqueness, we have added zeroth-
 402 order Tikhonov regularization to estimates of s and second-order Tikhonov regularization to
 403 estimates of effective fluidity η_{eff}^{-1} . The degree to which we impose the regularization on slip
 404 and fluidity is controlled by the penalty parameters λ_s and λ_η , which are chosen with trade-
 405 off curves (Figure S1). Our goal is to get a prior constraint on η_{eff} to minimize the amount
 406 of searching we have to do when describing the postseismic deformation over the full five years,
 407 which we do in Section 3.3. Estimates of s made here will not be used in Section 3.3, and
 408 so the motivation behind adding regularization to s is to ensure that the slip driving viscoelas-
 409 tic relaxation in eq. (14) is sensible.

410 Our initial estimate for coseismic slip and cumulative afterslip over the first 0.8 years
 411 after the El Mayor-Cucapah earthquake are shown in Figure 11. Similar to our elastic slip model
 412 from Section 3.1, a significant amount of right-lateral and normal coseismic slip is inferred
 413 to be on the Sierra Cucapah segment. Our coseismic slip solution on the Sierra Cucapah seg-
 414 ment is consistent with field studies [Fletcher *et al.*, 2014] and the model from Wei *et al.* [2011b].
 415 Our inferred slip on the Indiviso fault segment differs from Wei *et al.* [2011b] because the GPS
 416 data used in this study is not capable of resolving the spatial distribution of fault slip on that
 417 segment (Figure S2). The potency of inferred coseismic slip is $3.3 \times 10^9 \text{ m}^3$, which is also
 418 about the same as that inferred from Section 3.1. The present inference of afterslip on the In-
 419 diviso fault is significantly less than what was found in the Section 3.1 where we did not ac-
 420 count for viscoelasticity. When fault slip is simultaneously estimated with viscosity, the po-
 421 tency of inferred afterslip over the first 0.8 years after the earthquake is $0.85 \times 10^9 \text{ m}^3$, com-
 422 pared to $3.5 \times 10^9 \text{ m}^3$ when we assume the crust and upper mantle are elastic. The signifi-
 423 cant amount of afterslip inferred on the Indiviso fault seems to be compensating for unmod-
 424 eled viscoelastic relaxation. The fact that there is still an appreciable amount of afterslip in-
 425 ferred on the Indiviso fault raises the question of whether it is compensating for viscoelastic
 426 relaxation that is more localized than what we allow for since we only estimate depth depen-
 427 dent variations in viscosity.

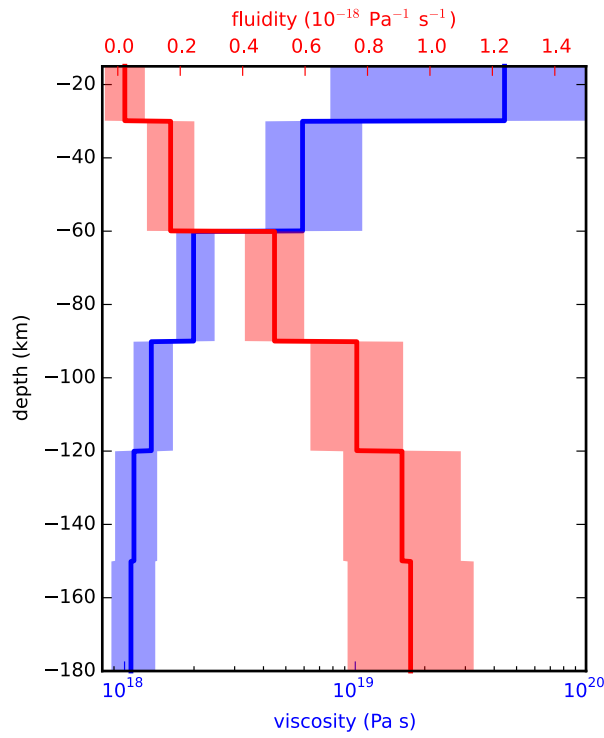
428 Our estimated effective viscosities, and corresponding fluidities, are shown in Figure 12.
 429 Although fluidity is rarely used in geophysical literature, eq. (13) is linear with respect to flu-
 430 idity and so the fluidity indicates the amplitude of the viscoelastic signal coming from each
 431 layer. We use bootstrapping to find the 95% confidence intervals for our estimated effective
 432 viscosities which are shown in Figure 12. It is important to remember that the presented ef-
 433 fective viscosities were estimated with a smoothing regularization constraint and so the un-
 434 certainties are almost certainly underestimated [Aster *et al.*, 2011]. Indeed, many viscosity pro-
 435 files which are outside of the shown confidence intervals can just as adequately described the
 436 first 0.8 years of postseismic deformation. Our solution in Figure 12 should be interpreted as
 437 the smoothest effective viscosity profile which is capable of describing the data. This means
 438 that any sharp viscosity transitions will be tapered out, which we demonstrate with a synthetic
 439 test in Figure S2. Nonetheless, a robust feature that we see is that the largest jump in fluid-
 440 ity is at 60 km depth, which is consistent with the range of lithosphere-asthenosphere bound-
 441 ary depths inferred by Lekic *et al.* [2011]. This transitional depth is also consistent with the
 442 the viscosity structure required to explain far-field postseismic deformation following the Hec-
 443 tor Mine earthquake [Freed *et al.*, 2007]. We find that the viscosity below 60 km depth needs
 444 to be $\sim 10^{18} \text{ Pa s}$ to describe the early rate of postseismic deformation at far-field stations while
 445 the lower crust and uppermost mantle need to be relatively stronger. The viscosity of the lower
 446 crust has the largest uncertainties because there is no evidence of relaxation in that layer, mean-
 447 ing that it is effectively elastic over the first 0.8 years after the earthquake.

453 3.3 Full Postseismic Inversion

454 In the previous section, we used the inverse method from Hines and Hetland [2016] to
 455 constrain the effective viscosity structure required to explain the first 0.8 years of postseismic
 456 deformation. In this section, we use these effective viscosities as a prior constraint when search-



448 **Figure 11.** Coseismic slip and afterslip inferred by fitting eq. (14) to the first 0.8 years of postseismic
449 displacements.



450 **Figure 12.** Effective viscosities and associated fluidities inferred by fitting eq. (14) to the first 0.8 years of
451 postseismic displacements. 95% confidence intervals, estimated from bootstrapping, are indicated by color
452 fields.

457 ing for models which are capable of describing the available five years of postseismic data,
 458 where our forward problem is now eq. (11) rather than the approximation given by eq. (14).
 459 We perform a series of fault slip inversions assuming a variety of rheologies for the lower crust
 460 and upper mantle which are consistent with our findings from Section 3.2. We appraise each
 461 model using the mean chi-squared value,

$$\bar{\chi}^2 = \frac{1}{N} \left\| \frac{u_{\text{pred}} - u_{\text{post}}}{\sigma_{\text{post}}} \right\|_2^2, \quad (16)$$

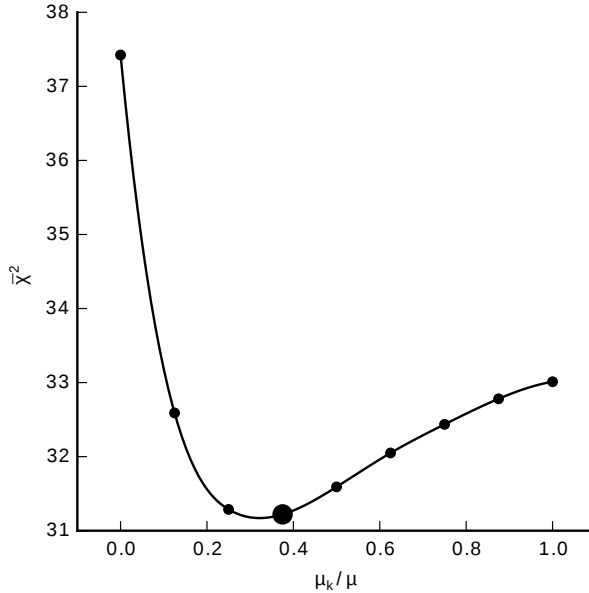
462 where N is the number of observations.

463 We first assume that the crust and mantle can be described with a Maxwell rheology,
 464 and we set the steady-state viscosity, η_M , equal to our inference of η_{eff} . We compute f and
 465 g from eq. (11) using Pylith, and we use the same spatial and temporal discretization of s as
 466 in Sections 3.1 and 3.2. We estimate s using linear least squares and find a misfit of $\bar{\chi}^2 =$
 467 37.4. For comparison, $\bar{\chi}^2 = 35.3$ for the elastic model from Section 3.1. The Maxwell vis-
 468 coelastic model has a larger misfit because it tends to overestimate the rate of deformation af-
 469 ter about three years (Figure 7). Since our initial estimates of η_{eff} may be biased towards over-
 470 estimating viscosities, we have also performed the slip inversion where we use uniformly lower
 471 viscosities in the crust and mantle. However, decreasing the viscosity only increases the mis-
 472 fit. Although, the viscosities used here are consistent with the successful Maxwell viscoelas-
 473 tic models found by *Rollins et al.* [2015] and *Spinler et al.* [2015], which had mantle viscosities
 474 on the order of 10^{18} Pa s and relatively higher lower crustal viscosities, we find that such
 475 a model is incapable of describing the entire postseismic time series. *Pollitz et al.* [2001] sim-
 476ilarly recognized this deficiency in a Maxwell rheology, which then motivated their exploration
 477 of a Burgers rheology upper mantle [*Pollitz*, 2003].

478 Instead of exploring a Burgers rheology mantle, which introduces two new parameters
 479 that need to be estimated, the transient viscosity, η_K , and transient shear modulus, μ_K , we first
 480 consider a Zener rheology for the mantle, which only introduces one additional unknown pa-
 481 rameter, μ_K . We assume that the lower crust still has a Maxwell rheology. The steady-state
 482 viscosity in the crust and the transient viscosity in the mantle are set equal to the inferred ef-
 483 fective viscosities. We then estimate the ratio of shear moduli, $\frac{\mu_K}{\mu}$. We compute nine differ-
 484 ent sets of Green's functions, f and g , where we assume values of $\frac{\mu_K}{\mu}$ ranging from 0 to 1.
 485 The former being a degenerate case where the Zener model reduces to the above Maxwell model.
 486 We estimate coseismic slip and afterslip for each realization of $\frac{\mu_K}{\mu}$. We find that a shear mod-
 487 uli ratio of 0.375 yields the best prediction to the observed postseismic displacements with a
 488 misfit of $\bar{\chi}^2 = 31.2$ (Figure 13). The improvement in the Zener model over the Maxwell model
 489 can be seen in the fit to the far-field data (Figure 7) where the Zener model does a significantly
 490 better job at explaining the transient rate of deformation throughout the five years considered
 491 in this study. The rheologic parameters for our preferred Zener model are summarized in Ta-
 492 ble 1.

493 Because we are able to adequately describe the available five years of postseismic de-
 494 formation with a Zener model, we do not find it necessary to explore the parameter space for
 495 a more complicated Burgers rheology. However, since the Zener model is a Burgers model with
 496 an infinite steady-state viscosity, we can conclude that any Burgers rheology that has a tran-
 497 sient viscosity consistent with that found in Section 3.2 and a steady-state viscosity $\gtrsim 10^{20}$
 498 Pa s, which is effectively infinite on the time scale of five years, would also be able to sat-
 499 isfactorily describe the observable postseismic deformation.

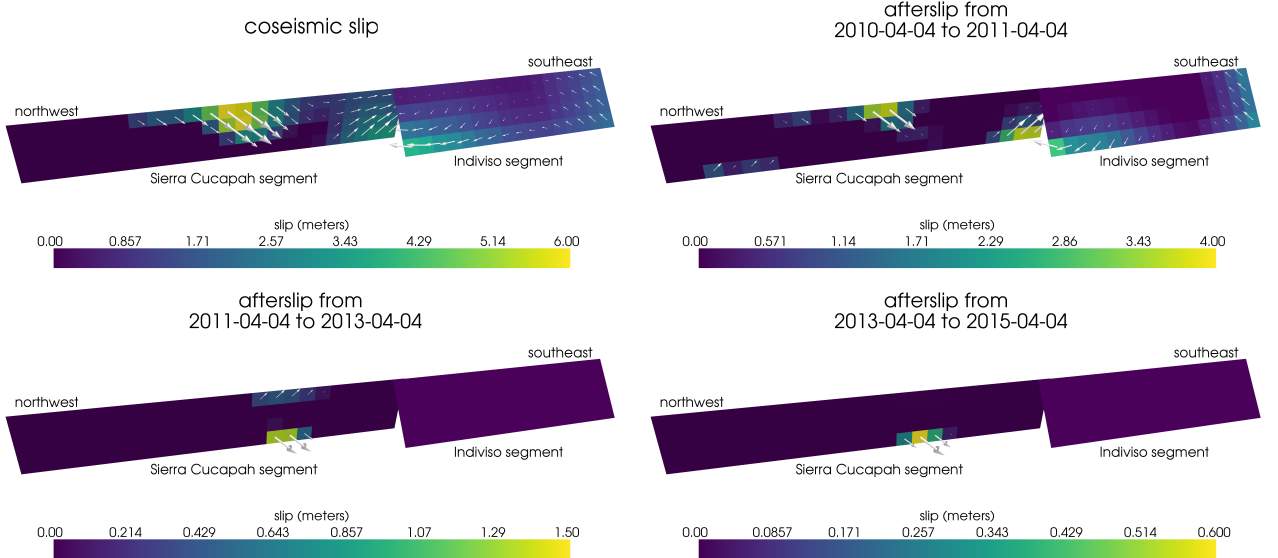
500 The regularized inference of coseismic slip and afterslip for our preferred Zener model
 501 is shown in Figure 14. The inferred coseismic potency is 3.0×10^9 m³, equivalent to a Mw=7.26
 502 earthquake, where most of the slip is shallow and on the Sierra Cucapah fault segment. The
 503 potency of five years of afterslip is 1.1×10^9 m³. Most of the afterslip in our preferred model
 504 occurs within the first year after the earthquake and coincides with the location of our inferred
 505 coseismic slip. Inferred afterslip within the first year is accounting for the most rapid near-



493 **Figure 13.** Mean chi-squared value for the best fitting slip model as a function of the transient shear modu-
 494 lus relative to the elastic shear modulus in a Zener upper mantle. Large dot indicates our preferred ratio.

508 field transient deformation. After one year, afterslip is inferred to be deeper down on the Sierra
 509 Cucapah segment, which is describing much of the sustained near-field postseismic deforma-
 510 tion. We emphasize, that the GPS station closest to where we infer afterslip, P496, is still about
 511 30 km away, which is too far for us to conclusively argue for sustained localized deformation
 512 rather than shallow distributed deformation. The deep afterslip inferred after one year could
 513 potentially be describing deformation resulting from lower crustal flow. To test this, we have
 514 modified our preferred model by decreasing the lower crustal viscosity from 5.91×10^{19} Pa
 515 s to 1×10^{19} Pa s, which is still consistent with our viscosity inference from Section 3.2, and
 516 we inverted for fault slip. We find that a model with a weaker lower crust adequately describes
 517 the postseismic displacements without any afterslip after one year, while still requiring about
 518 the same amount of afterslip over the first year. We do believe that the early, shallow after-
 519 slip on the Sierra Cucapah segment is a robust feature in our preferred model, while we are
 520 not confident in our inference of later deep afterslip.

521 The postseismic displacements predicted by our preferred Zener model are shown in Fig-
 522 ures 4, 5 and 7. Overall, the trends in the near-field and far-field deformation is better described
 523 by our preferred Zener model than either an elastic model or a model with a Maxwell viscoelas-
 524 tic mantle. The largest residuals occur within the Imperial Valley and these residuals do not
 525 appear to have any systematic trend. This suggests that the large errors are due to localized
 526 processes such as fault slip in the Imperial Valley triggered by the El Mayor-Cucapah earth-
 527 quake [Wei *et al.*, 2011a, 2015]. We do not see any pattern in the residuals that would suggest
 528 a laterally heterogeneous viscosity structure, which has been explored by Pollitz *et al.* [2012]
 529 and Rollins *et al.* [2015]. As discussed in section 2, our method for data processing is not able
 530 to completely remove the seasonal signal in the GPS data and this results in regionally uni-
 531 form oscillations in the lateral and vertical components of the residuals with an amplitude of
 532 1-2 millimeters. Additionally, we see systematic misfit in the later postseismic period west of
 533 the Landers and Hector Mine earthquakes, which may be the result of unmodeled postseis-
 534 mic deformation resulting from those earthquakes. Lastly, there are clear discrepancies between
 535 the observed and predicted vertical deformation following the first year after the El Mayor Cu-
 536 capah earthquake. We observe a broad uplift throughout Southern California, which is incon-
 537 sistent with any postseismic model.



538 **Figure 14.** Inferred coseismic slip and afterslip when assuming a Maxwell rheology in the lower crust and
 539 a Zener rheology in the upper mantle. The transient viscosity η_K in the mantle and steady-state viscosity η_M
 540 in the crust are set equal to the effective viscosities from Figure 12. We set $\frac{\mu_K}{\mu} = 0.375$ in the upper mantle.

541 4 Discussion

542 It has long been recognized that deep afterslip and viscoelastic relaxation following an
 543 upper crustal earthquake can result in similar horizontal ground deformation at the surface [e.g.
 544 *Savage*, 1990; *Pollitz et al.*, 2001; *Hearn*, 2003; *Feigl and Thatcher*, 2006]. The similarity of
 545 the horizontal postseismic deformation results in a non-uniqueness in inferences of afterslip
 546 or viscoelastic relaxation. In contrast, the spatial pattern of vertical postseismic deformation
 547 has been proposed to be a discriminant between deep afterslip and viscoelastic relaxation [e.g.
 548 *Pollitz et al.*, 2001; *Hearn*, 2003]. It is, however, important to note that patterns of vertical de-
 549 formation are very sensitive to the depth-dependence of viscosity below the upper crust [*Yang*
 550 and *Toksöz*, 1981; *Hetland and Zhang*, 2014]. The similarity between deformation resulting
 551 from deep afterslip and viscoelastic relaxation of coseismic stresses is different from the ill-
 552 posedness described in Section 3.2. In our method, any inferred afterslip will also mechani-
 553 cally drive additional viscoelastic relaxation. The horizontal deformation resulting from deep
 554 afterslip will generally be in the opposite direction as horizontal deformation resulting from
 555 viscoelastic relaxation of subsequent stresses in the lower crust (Figure 9). As a result, there
 556 is a trade-off between inferences of deep afterslip and lower crustal viscosity. In our synthetic
 557 tests in *Hines and Hetland* [2016], we have found that inverting surface deformation for af-
 558 terslip and viscosity within the same depth interval tends to result in overestimated afterslip
 559 and an underestimated viscosity.

560 Most postseismic studies assume Maxwell viscoelasticity in the lower crust and upper
 561 mantle [e.g. *Nur and Mavko*, 1974; *Pollitz et al.*, 2000; *Hetland*, 2003; *Freed et al.*, 2006; *John-*
 562 *son et al.*, 2009; *Hearn et al.*, 2009], which is the simplest viscoelastic rheologic model. In South-
 563 ern California, postseismic studies following the Landers [*Pollitz et al.*, 2000], Hector Mine
 564 [*Pollitz et al.*, 2001], and El Mayor-Cucapah earthquake [*Spinler et al.*, 2015; *Rollins et al.*, 2015],
 565 have assumed Maxwell viscoelasticity in the lower crust and upper mantle and have inferred
 566 upper mantle viscosities on the order of 10^{17} to 10^{18} Pa s and lower crust viscosities $\gtrsim 10^{19}$
 567 Pa s. These postseismic studies are consistent with *Kaufmann and Amelung* [2000] and *Cav-*
 568 *alié et al.* [2007], who found that an upper mantle viscosity of 10^{18} Pa s and a crustal viscos-

569 ity $\gtrsim 10^{20}$ Pa s are necessary to describe subsidence resulting from changes in loading from
 570 Lake Mead. This isostatic adjustment is a process with similar spatial and temporal scales as
 571 postseismic deformation, and thus the inferred viscosities of these two types of studies would
 572 likely agree. While these studies found viscosities that are consistent with our effective vis-
 573 cosities from Section 3.2, they are inconsistent with viscosity estimates made from geophys-
 574 ical processes that occur over longer time scales. For example, *Lundgren et al.* [2009] found
 575 that lower crust and upper mantle viscosities on the order of 10^{21} and 10^{19} Pa s, respectively,
 576 are needed to describe interseismic deformation along the Southern San Andreas fault zone
 577 in the Salton Sea region. An even higher mantle viscosity, on the order of 10^{20} Pa s, is re-
 578 quired to describe isostatic adjustment resulting from the draining of Lake Bonneville, which
 579 occurs on the time scales of 10^4 years [*Crittenden*, 1967; *Bills and May*, 1987].

580 An additional deficiency with the Maxwell rheology is that it predicts a steady decay
 581 in the rate of postseismic deformation over time, which fails to describe the commonly ob-
 582 served rapid, early transience followed by a relatively steady rate of postseismic deformation.
 583 One could explain the early transient postseismic deformation with fault creep and the later
 584 phase with relaxation in a Maxwell viscoelastic lower crust and upper mantle [e.g *Hearn et al.*,
 585 2009; *Johnson et al.*, 2009]. However, postseismic deformation at distances greater than ~ 200
 586 km from the El Mayor-Cucapah epicenter can only be attributed to viscoelastic relaxation [*Freed*
 587 *et al.*, 2007] and we have demonstrated that the far-field deformation cannot be explained with
 588 a Maxwell rheology (Figure 7).

589 We found that a Zener rheology in the upper mantle with a transient viscosity of $\sim 10^{18}$
 590 Pa s does a noticeably better job at predicting far-field postseismic deformation. A general-
 591 ization of the Zener viscoelastic model, schematically represented as several Kelvin elements
 592 connected in series, is commonly used to describe seismic attenuation [*Liu et al.*, 1976]. The
 593 highest viscosity needed to describe seismic attenuation is on the order of 10^{16} Pa s [*Yuen and*
 594 *Peltier*, 1982] which has a characteristic relaxation time on the order of days. Even though
 595 our inferred transient viscosity is orders of magnitude larger than that required for seismic at-
 596 tenuation models, the two models are not incompatible. Rather, the delayed elasticity in seis-
 597 mic attenuation models occurs on such short time scales that it can be considered part of the
 598 instantaneous elastic phase of deformation associated with the preferred Zener model in this
 599 study.

600 Of course, a Zener rheology provides an incomplete descriptions of the asthenosphere,
 601 as it does not have the fluid-like behavior required to explain isostatic rebound or convection
 602 in the mantle [*O'Connell*, 1971]. *Yuen and Peltier* [1982] proposed a Burgers rheology with
 603 a low transient viscosity ($\eta_K \approx 10^{16}$ Pa s) and high steady-state viscosity ($\eta_M \approx 10^{21}$ Pa
 604 s) to describe both seismic attenuation and long term geologic processes. The justification of
 605 a Burger's rheology mantle is further supported by laboratory experiments on olivine [*Chopra*,
 606 1997]. *Pollitz* [2003] sought to describe postseismic deformation following Hector Mine with
 607 a Burgers rheology mantle and they found a best fitting transient viscosity of 1.6×10^{17} Pa
 608 s and steady-state viscosity of 4.6×10^{18} Pa s. While the Burgers rheology was introduced
 609 as a means of bridging the gap between relaxation observed in long and short term geophys-
 610 ical processes, the inferred steady state viscosity from *Pollitz* [2003] is still inconsistent with
 611 the Maxwell viscosities inferred from studies on the earthquake cycle and Lake Bonneville.
 612 The transient viscosity inferred by *Pollitz* [2003] is constrained by the earliest phase of post-
 613 seismic deformation following the Hector Mine earthquake. While *Pollitz* [2003] ruled out deep
 614 afterslip as an alternative mechanism based on inconsistent vertical deformation, it is still pos-
 615 sible to successfully describe all components of early postseismic deformation following the
 616 Hector Mine earthquake with afterslip at seismogenic depths [*Jacobs et al.*, 2002]. It is then
 617 possible that the preferred rheologic model from *Pollitz* [2003] was biased towards inferring
 618 a particularly low transient viscosity by neglecting to account for afterslip. This is in contrast
 619 to the present study, where we have inferred a viscosity structure simultaneously with after-
 620 slip. We also argue that a transient rheology is necessary to explain postseismic deformation;
 621 however, our preferred transient viscosity of $\sim 10^{18}$ Pa s in the upper mantle is an order of mag-

622 nitude larger than the transient viscosity found by *Pollitz* [2003]. The transient viscosity in-
 623 ferred here is consistent with the results of *Pollitz* [2015], who reanalyzed postseismic data
 624 following the Landers and Hector Mine earthquake allowing the first few months of transient
 625 deformation to be described by afterslip. Since a Zener model is able to describe the avail-
 626 able postseismic deformation following the El Mayor-Cucapah earthquake, any Burgers rhe-
 627 ology with a steady-state viscosity that is $\gtrsim 10^{20}$ Pa s, effectively infinite over five years, would
 628 also be able to describe the postseismic deformation. Such a Burgers model might then be con-
 629 sistent with the steady-state viscosities necessary for lake loading, interseismic deformation,
 630 and mantle dynamics.

631 5 Conclusion

632 We have extracted a smoothed estimate of postseismic deformation following the El Mayor-
 633 Cucapah earthquake from GPS displacement time series. Our estimated postseismic deforma-
 634 tion reveals far-field (epicentral distances $\gtrsim 200$ km) transient deformation which is undetectable
 635 after about three years. Near-field deformation exhibits transience that decays to a sustained,
 636 elevated rate after about one or two years. We found that near-field transient deformation can
 637 be explained with shallow afterslip, and the sustained rate of near-field deformation can ei-
 638 ther be explained with continued afterslip or viscoelastic relaxation in the lower crust. Far-field
 639 transient deformation can be more definitively ascribed to viscoelastic relaxation at depths greater
 640 than ~ 60 km. Beneath that depth, a transient viscosity of $\sim 10^{18}$ Pa s is required to describe
 641 the rate of far-field deformation throughout the five years considered in this study. By describ-
 642 ing the available postseismic deformation with a transient rheology in the mantle, our preferred
 643 model does not conflict with the generally higher steady-state viscosities inferred from geo-
 644 physical processes occurring over longer time scales.

645 Acknowledgements

646 We thank Andy Freed for an illuminating discussion on the data used in this study. This
 647 material is based on EarthScope Plate Boundary Observatory data services provided by UN-
 648 AVCO through the GAGE Facility with support from the National Science Foundation (NSF)
 649 and National Aeronautics and Space Administration (NASA) under NSF Cooperative Agree-
 650 ment No. EAR-1261833. The data used in this study can be found at www.unavco.org. This
 651 material is based upon work supported by the National Science Foundation under Grant Num-
 652 bers EAR 1045372 and EAR 1245263.

653 References

- 654 Aagaard, B. T., M. G. Knepley, and C. A. Williams (2013). A domain decomposition
 655 approach to implementing fault slip in finite-element models of quasi-static and dy-
 656 namic crustal deformation, *Journal of Geophysical Research: Solid Earth*, 118, doi:
 657 10.1002/jgrb.50217.
- 658 Argus, D. F., M. B. Heflin, G. Peltzer, F. Crampé, and F. H. Webb (2005), Interseismic
 659 strain accumulation and anthropogenic motion in metropolitan Los Angeles, *Journal of*
 660 *Geophysical Research: Solid Earth*, 110(4), 1–26, doi:10.1029/2003JB002934.
- 661 Aster, R. C., B. Borchers, and C. H. Thurber (2011), Parameter Estimation and Inverse
 662 Problems, vol. 90, Academic Press.
- 663 Bawden, G. W., W. Thatcher, R. S. Stein, K. W. Hudnut, and G. Peltzer (2001), Tectonic
 664 contraction across Los Angeles after removal of groundwater pumping effects., *Nature*,
 665 412(August), 812–815, doi:10.1038/35090558.
- 666 Bills, B. G., and G. M. May (1987), Lake Bonneville: Constraints on Lithospheric Thick-
 667 ness and Upper Mantle Viscosity From Isostatic Warping of Bonneville, Provo, and
 668 Gilbert Stage Shorelines, *Journal of Geophysical Research-Solid Earth and Planets*,
 669 92(B11), 11,493–11,508, doi:10.1029/JB092iB11p11493.

- 670 Çakir, Z., S. Ergintav, H. Özener, U. Dogan, A. M. Akoglu, M. Meghraoui, and
 671 R. Reilinger (2012), Onset of aseismic creep on major strike-slip faults, *Geology*,
 672 40(12), 1115–1118, doi:10.1130/G33522.1.
- 673 Cavalié, O., M. P. Doin, C. Lasserre, and P. Briole (2007), Ground motion measurement in
 674 the Lake Mead area, Nevada, by differential synthetic aperture radar interferometry time
 675 series analysis: Probing the lithosphere rheological structure, *Journal of Geophysical*
 676 *Research: Solid Earth*, 112(3), 1–18, doi:10.1029/2006JB004344.
- 677 Cetin, E., Z. Çakir, M. Meghraoui, S. Ergintav, and A. M. Akoglu (2014), Extent and
 678 distribution of aseismic slip on the Ismetpasa segment of the North Anatolian Fault
 679 (Turkey) from Persistent Scatterer InSAR, *Geochemistry, Geophysics, Geosystems*, 15,
 680 doi:10.1002/2014GC005307.Received.
- 681 Chopra, P. N. (1997), High-temperature transient creep in olivine rocks, *Tectonophysics*,
 682 279, 93–111, doi:10.1016/S0040-1951(97)00134-0.
- 683 Crittenden, M. (1967), Viscosity and Finite Strength of the Mantle as Determined from
 684 Water and Ice Loads*, *Geophysical Journal of the Royal Astronomical* ..., pp. 261–279,
 685 doi:10.1111/j.1365-246X.1967.tb06243.x.
- 686 Davis, J. L., B. P. Wernicke, and M. E. Tamisiea (2012), On seasonal signals in geode-
 687 tic time series, *Journal of Geophysical Research: Solid Earth*, 117(1), 1–10, doi:
 688 10.1029/2011JB008690.
- 689 Feigl, K. L., and W. Thatcher (2006), Geodetic observations of post-seismic transients in
 690 the context of the earthquake deformation cycle, *Comptes Rendus - Geoscience*, 338,
 691 1012–1028, doi:10.1016/j.crte.2006.06.006.
- 692 Fletcher, J. M., O. J. Teran, T. K. Rockwell, M. E. Osokin, K. W. Hudnut, K. J. Mueller,
 693 R. M. Spelz, S. O. Akciz, E. Masana, G. Faneros, E. J. Fielding, S. Leprince, A. E.
 694 Morelan, J. Stock, D. K. Lynch, A. J. Elliott, P. Gold, J. Liu-Zeng, A. González-
 695 Ortega, A. Hinojosa-Corona, and J. González-García (2014), Assembly of a large
 696 earthquake from a complex fault system: Surface rupture kinematics of the 4 April
 697 2010 El Mayor-Cucapah (Mexico) Mw 7.2 earthquake, *Geosphere*, 10(4), 797–827,
 698 doi:10.1130/GES00933.1.
- 699 Freed, A. M., R. Bürgmann, E. Calais, J. Freymueller, and S. Hreinsdóttir (2006), Impli-
 700 cations of deformation following the 2002 Denali, Alaska, earthquake for postseismic
 701 relaxation processes and lithospheric rheology, *Journal of Geophysical Research: Solid*
 702 *Earth*, 111, 1–23, doi:10.1029/2005JB003894.
- 703 Freed, A. M., R. Bürgmann, and T. Herring (2007), Far-reaching transient motions after
 704 Mojave earthquakes require broad mantle flow beneath a strong crust, *Geophysical*
 705 *Research Letters*, 34, 1–5, doi:10.1029/2007GL030959.
- 706 Gonzalez-Ortega, A., Y. Fialko, D. Sandwell, F. A. Nava-pichardo, J. Fletcher,
 707 J. Gonzalez-garcia, B. Lipovsky, M. Floyd, and G. Funning (2014), El Mayor-
 708 Cucapah (Mw7.2) earthquake: early near-field postseismic deformation from In-
 709 Sar and GPS observations, *Journal of Geophysical Research*, 119, 1482–1497, doi:
 710 10.1002/2013JB010193.Received.
- 711 Hauksson, E., J. Stock, K. Hutton, W. Yang, J. A. Vidal-Villegas, and H. Kanamori
 712 (2011), The 2010 Mw 7.2 El mayor-cucapah earthquake sequence, Baja Califor-
 713 nia, Mexico and Southernmost California, USA: Active seismotectonics along the
 714 Mexican pacific margin, *Pure and Applied Geophysics*, 168(3918), 1255–1277, doi:
 715 10.1007/s00024-010-0209-7.
- 716 Hearn, E. H. (2003), What can GPS data tell us about the dynamics of post-seismic defor-
 717 mation ?, (2003), 753–777.
- 718 Hearn, E. H., S. McClusky, S. Ergintav, and R. E. Reilinger (2009), Izmit earthquake post-
 719 seismic deformation and dynamics of the North Anatolian Fault Zone, *Journal of Geo-*
 720 *physical Research: Solid Earth*, 114(August 2008), 1–21, doi:10.1029/2008JB006026.
- 721 Hetland, E. A. (2003), Postseismic relaxation across the Central Nevada Seismic Belt,
 722 *Journal of Geophysical Research*, 108(Figure 2), 1–13, doi:10.1029/2002JB002257.

- Hetland, E. A., and G. Zhang (2014), Effect of shear zones on post-seismic deformation with application to the 1997 Mw 7.6 manyi earthquake, *Geophysical Journal International*, **198**, 259–269, doi:10.1093/gji/ggu127.
- Hines, T. T., and E. A. Hetland (2013), Bias in estimates of lithosphere viscosity from interseismic deformation, *Geophysical Research Letters*, **40**(16), 4260–4265, doi:10.1002/grl.50839.
- Hines, T. T., and E. A. Hetland (2016), Rapid and simultaneous estimation of fault slip and heterogeneous lithospheric viscosity from post-seismic deformation, *Geophysical Journal International*, **204**(1), 569–582, doi:10.1093/gji/ggv477.
- Jacobs, A., D. Sandwell, Y. Fialko, and L. Sichoux (2002), The 1999 (Mw7.1) Hector Mine, California, Earthquake: Near-Field Postseismic Deformation from ERS Interferometry, *Bulletin of the Seismological Society of America*, **92**(May), 1433–1442.
- Johnson, K. M., and P. Segall (2004), Viscoelastic earthquake cycle models with deep stress-driven creep along the San Andreas fault system, *Journal of Geophysical Research: Solid Earth*, **109**, 1–19, doi:10.1029/2004JB003096.
- Johnson, K. M., R. Bürgmann, and J. T. Freymueller (2009), Coupled afterslip and viscoelastic flow following the 2002 Denali Fault, Alaska earthquake, *Geophysical Journal International*, **176**(3), 670–682, doi:10.1111/j.1365-246X.2008.04029.x.
- Jónsson, S., P. Segall, R. Pedersen, and G. Bjornsson (2003), Post-earthquake ground movements correlated to pore-pressure transients, *Nature*, **424**(July), 179–183, doi:10.1038/nature01758.1.
- Kaufmann, G., and F. Amelung (2000), Reservoir-induced deformation and continental rheology in vicinity of Lake Mead, Nevada, *Journal of Geophysical Research*, **105**(B7), 16,341, doi:10.1029/2000JB900079.
- Kroll, K. A., E. S. Cochran, K. B. Richards-Dinger, and D. F. Sumy (2013), Aftershocks of the 2010 Mw 7.2 El Mayor-Cucapah earthquake reveal complex faulting in the Yuha Desert, California, *Journal of Geophysical Research: Solid Earth*, **118**(October), 6146–6164, doi:10.1002/2013JB010529.
- Lekic, V., S. W. French, and K. M. Fischer (2011), Lithospheric Thinning Beneath Rifted Regions of Southern California, *Science*, **334**(November), 783–787.
- Liu, H.-P., D. L. Anderson, and H. Kanamori (1976), Velocity dispersion due to anelasticity; implications for seismology and mantle composition, *Geophysical Journal International*, **47**(1), 41–58, doi:10.1111/j.1365-246X.1976.tb01261.x.
- Lundgren, P., E. A. Hetland, Z. Liu, and E. J. Fielding (2009), Southern San Andreas-San Jacinto fault system slip rates estimated from earthquake cycle models constrained by GPS and interferometric synthetic aperture radar observations, *Journal of Geophysical Research: Solid Earth*, **114**(2), 1–18, doi:10.1029/2008JB005996.
- McGuire, J. J., and P. Segall (2003), Imaging of aseismic fault slip transients recorded by dense geodetic networks, *Geophysical Journal International*, **155**(3), 778–788, doi:10.1111/j.1365-246X.2003.02022.x.
- Meade, B. J., and B. H. Hager (2005), Block models of crustal motion in southern California constrained by GPS measurements, *Journal of Geophysical Research B: Solid Earth*, **110**, 1–19, doi:10.1029/2004JB003209.
- Murray, J. R., and P. Segall (2005), Spatiotemporal evolution of a transient slip event on the San Andreas fault near Parkfield, California, *Journal of Geophysical Research : Solid Earth*, **110**(9), 1–12, doi:10.1029/2005JB003651.
- Nur, A., and G. Mavko (1974), Postseismic viscoelastic rebound, *Science*, **183**(4121), 204–206, doi:10.1038/098448b0.
- O'Connell, R. J. (1971), Rheology of the Mantle, *EOS, Transactions, American Geophysical Union*, **52**, 140–142.
- Oskin, M. E., J. R. Arrowsmith, A. Hinojosa Corona, A. J. Elliott, J. M. Fletcher, E. J. Fielding, P. O. Gold, J. J. Gonzalez Garcia, K. W. Hudnut, J. Liu-Zeng, and O. J. Teran (2012), Near-field deformation from the El Mayor-Cucapah earthquake revealed by differential LIDAR, *Science*, **335**(6069), 702–705, doi:10.1126/science.1213778.

- Pollitz, F., C. Wicks, and W. Thatcher (2001), Mantle Flow Beneath a Continental Strike-Slip Fault : Postseismic Deformation After the 1999 Hector Mine Earthquake, *Science*, 1814(2001), 1814–1818, doi:10.1126/science.1061361.
- Pollitz, F. F. (2003), Transient rheology of the uppermost mantle beneath the Mojave Desert, California, *Earth and Planetary Science Letters*, 215, 89–104, doi: 10.1016/S0012-821X(03)00432-1.
- Pollitz, F. F., G. Peltzer, and R. Bürgmann (2000), Mobility of continental mantle: Evidence from postseismic geodetic observations following the 1992 Landers earthquake, *Journal of Geophysical Research*, 105(1999), 8035, doi:10.1029/1999JB900380.
- Pollitz, F. F., R. Bürgmann, and W. Thatcher (2012), Illumination of rheological mantle heterogeneity by the M7.2 2010 El Mayor-Cucapah earthquake, *Geochemistry, Geophysics, Geosystems*, 13(6), 1–17, doi:10.1029/2012GC004139.
- Pollitz, F. F. (2015). Postearthquake relaxation evidence for laterally variable viscoelastic structure and water content in the Southern California mantle, *Journal of Geophysical Research: Solid Earth*, 120, 2672–2696, doi:10.1002/2014JB011603.
- Rauch, H. E., F. Tung, and C. T. Striebel (1965), Maximum likelihood estimates of linear dynamic systems, *AIAA Journal*, 3(8), 1445–1450.
- Riva, R. E. M., and R. Govers (2009), Relating viscosities from postseismic relaxation to a realistic viscosity structure for the lithosphere, *Geophysical Journal International*, 176, 614–624, doi:10.1111/j.1365-246X.2008.04004.x.
- Rollins, C., S. Barbot, and J.-P. Avouac (2015), Postseismic Deformation Following the 2010 M7.2 El Mayor-Cucapah Earthquake : Observations , Kinematic Inversions , and Dynamic Models, *Pure and Applied Geophysics*, doi:10.1007/s00024-014-1005-6.
- Savage, J. C. (1990), Equivalent strike-slip earthquake cycles in half-space and lithosphere-asthenosphere earth models, *Journal of Geophysical Research*, 95, 4873, doi:10.1029/JB095iB04p04873.
- Savage, J. C., and J. L. Svart (2009), Postseismic relaxation following the 1992 M 7.3 Landers and 1999 M 7.1 Hector Mine earthquakes , southern California, *Journal of Geophysical Research*, 114(B01401), doi:10.1029/2008JB005938.
- Savage, J. C., J. L. Svart, and S. B. Yu (2005), Postseismic relaxation and transient creep, *Journal of Geophysical Research: Solid Earth*, 110, 1–14, doi:10.1029/2005JB003687.
- Segall, P., and M. Mathews (1997), Time dependent inversion of geodetic data, *Journal of Geophysical Research*, 102.
- Spinler, J. C., R. A. Bennett, C. Walls, L. Shawn, and J. J. G. Garcia (2015), Assessing long-term postseismic deformation following the M7.2 4 April 2010, El Mayor-Cucapah earthquake with implications for lithospheric rheology in the Salton Trough, *Journal of Geophysical Research: Solid Earth*, 120, 3664–3679, doi: 10.1002/2014JB011613.Received.
- Wei, M., D. Sandwell, Y. Fialko, and R. Bilham (2011a), Slip on faults in the Imperial Valley triggered by the 4 April 2010 Mw 7.2 El Mayor-Cucapah earthquake revealed by InSAR, *Geophysical Research Letters*, 38(January), 1–6, doi:10.1029/2010GL045235.
- Wei, M., Y. Liu, Y. Kaneko, J. J. McGuire, and R. Bilham (2015), Dynamic triggering of creep events in the Salton Trough, Southern California by regional M5.4 earthquakes constrained by geodetic observations and numerical simulations, *Earth and Planetary Science Letters*, 427, 1–10, doi:10.1016/j.epsl.2015.06.044.
- Wei, S., E. Fielding, S. Leprince, A. Sladen, J.-P. Avouac, D. Helmberger, E. Hauksson, R. Chu, M. Simons, K. Hudnut, T. Herring, and R. Briggs (2011b), Superficial simplicity of the 2010 El MayorCucapah earthquake of Baja California in Mexico, *Nature Geoscience*, 4(9), 615–618, doi:10.1038/ngeo1213.
- Yang M., and M. N. Toksöz (1981), Time-dependent deformation and stress relaxation after strike-slip earthquakes, *Journal of Geophysical Research*, 86, 2889–2901.
- Yuen, D. A., and W. R. Peltier (1982), Normal modes of the viscoelastic earth, *Geophysical Journal of the Royal Astronomical Society*, 69, 495–526, doi:10.1111/j.1365-246X.1982.tb04962.x.